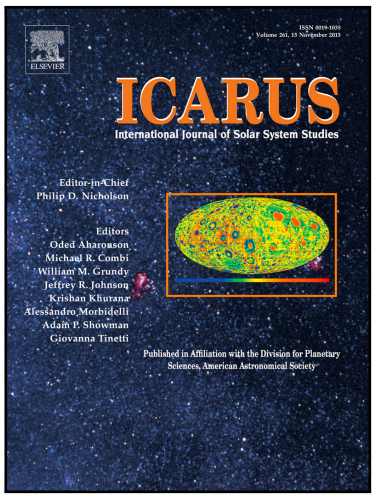

Variability and geologic associations of volcanic activity in 2001-2016

Clayton Cantrall, Katherine de Kleer, Imke de Pater,
David A. Williams, Ashley Gerard Davies, David Nelson

PII: S0019-1035(17)30501-8
DOI: 10.1016/j.icarus.2018.04.007
Reference: YICAR 12863

To appear in: *Icarus*

Received date: 8 July 2017
Revised date: 11 March 2018
Accepted date: 10 April 2018

Please cite this article as: Clayton Cantrall, Katherine de Kleer, Imke de Pater, David A. Williams, Ashley Gerard Davies, David Nelson, Variability and geologic associations of volcanic activity in 2001-2016, *Icarus* (2018), doi: 10.1016/j.icarus.2018.04.007

Highlights

- We present a compiled dataset of adaptive optic observations of Io between 2001 and 2016.
- Geologic associations of active volcanic sources are made using the USGS map of Io.
- The spatial distribution of active thermal sources and global heat flux has remained relatively constant over decadal timescales.
- Regional variations in the global heat flux exist on monthly to yearly timescales.

Variability and geologic associations of volcanic activity in 2001-2016

Clayton Cantrall[1], Katherine de Kleer[2, 3], Imke de Pater[2, 4], David A. Williams[5], Ashley Gerard Davies[6], David Nelson[5]

[1] *Aerospace Engineering Sciences Department, University of Colorado, Boulder, CO 80309, USA,*
[2] *Astronomy Department, 501 Campbell Hall, University of California, Berkeley, CA 94720, USA,*
[3] *Division of Geological and Planetary Sciences, California Institute of Technology, Pasadena, CA 91125,*
[4] *Faculty of Aerospace Engineering, Delft University of Technology, NL-2629 HS Delft, The Netherlands,*
[5] *School of Earth and Space Exploration, Arizona State University, Tempe, AZ 85287, USA,*
[6] *Jet Propulsion Laboratory, California Institute of Technology, 4800 Oak Grove Drive, Pasadena, CA 91109, USA*

Clayton Cantrall
Department of Aerospace Engineering Sciences
University of Colorado, Boulder
Boulder, CO 80309
Clayton.Cantrall@colorado.edu

Keywords: Io, Volcanism, Infrared Observations

1 Abstract

Since the end of the *Galileo* epoch, ground-based observations have been crucial for the continued monitoring and characterization of volcanic activity on Jupiter's moon, Io. We compile and analyze observations from the Keck and Gemini North telescopes between 2001 and 2016, including new and published observations from 2003, 2004, 2005, 2007, 2008, 2009, 2011, 2012, 2013, and 2016. A total of 88 distinct hot spot sites were detected over the 15-year period, 82 of which were detected multiple times, and 24 of which were not detected by *Galileo* at thermal infrared wavelengths (1-5 μm). A variety of analytical methods are utilized to investigate the detections of active volcanism as a surface expression of interior heating. Geologic associations of hot spots, including patera type, lava flow type, and proximity to mountainous regions, are made using the USGS-published global geologic map of Io (Williams et al. 2011a). We also provide a summary of outburst-scale events, along with the slightly less bright but more frequent, mini-outbursts described by de Kleer and de Pater (2016a).

We investigate the spatial distribution of volcanic activity on Io using nearest neighbor, mean pairwise spacing, and mean latitude statistics with various classification schemes. The analysis confirms previous findings in that the heat dissipation appears to be primarily concentrated in the asthenosphere resulting in a high time-averaged surface heat flux at low latitudes. Our observations show significant spatial deviations do exist from the asthenosphere heat dissipation model while also suggesting a deeper source of magma ascent to be present as well, supporting conclusions from previous analyses of primarily spacecraft data (Veeder et al., 2012; Hamilton et al., 2013; Davies et al., 2015). From a temporal perspective, there are signs of significant variations in the distribution of global heat flux, as volcanoes undetected, and probably dormant, during the *Galileo* encounters subsequently erupted and remained active during our observations. We also use the on 3.8-μm radiant intensity timelines of individual hot spots, along with the distribution of extensive lava fields in relation to detected activity, as a means to investigate possible connections between hot spots and short timescale, spatio-temporal variations in the global heat flux distribution. We conclude that while the global heat flux distribution remains relatively constant over decadal timescales, there is evidence that significant deviations do occur potentially as a result of mountain forming processes or triggering mechanisms between eruptions.

2 Introduction

The prolific volcanic activity on Jupiter's moon, Io, has been a well-documented phenomenon since the first surface images provided by the *Voyager* mission (Smith et al., 1979). The global heat flow of Io, calculated to be between 1.9 and 2.6 W/m2 (Matson et al., 1981; Veeder et al., 1994, 2012), is most likely a result of tidal heating resulting from Io's forced eccentric orbit around Jupiter (Peale et al., 1979). The heat transfer from this tidal forcing occurs primarily through advection, spurring the high-rate of volcanism observed at the surface.

The *Galileo* mission provided the first detailed view of Io's volcanism over a five-and-a-half-year period beginning in June 1996. Among many valuable insights, the imagery and data acquired from the Solid-State Imager (SSI) (Belton et al., 1992), Near-Infrared Mapping Spectrometer (NIMS) (Carlson et al., 1992), and Photopolarimeter-Radiometer (PPR) (Russell et al., 1992) demonstrated the wide variety and high variability of eruptions on Io, while also providing a never before seen view into the surface geology associated with these eruptions. Since *Galileo*, ground-based observations have added to the timeline of Io's volcanic activity. Using the Keck and Gemini North telescopes coupled with adaptive optics, we can resolve individual eruptions on the surface of Io in the near-infrared, enabling us to continue monitoring the characteristics and locations of hot spots from the ground.

We present near-infrared adaptive optics observations of Io obtained between 2001 and 2016, some of which were previously published (Marchis et al. 2005; de Pater et al. 2014a; 2016a; 2016b; de Kleer and de Pater 2016a;b). We analyze the spatial and temporal variability of the thermal detections in the adaptive optics dataset. We therefore add to the timeline of Io's evolving volcanic activity. Io displays a variety of eruption styles (e.g., Davies, 2007), but none more notable than the outburst-scale events, where the total radiance of Io in Ms-band (5 μm) doubles at the peak of the event (Blaney et al., 1995). A summary of these eruptions detected during the adaptive optics program, along with mini-outburst eruptions, is provided. Previous outbursts are summarized by Veeder et al. (2012) and references therein. We also investigate the geologic associations of the detections within the Io database, built in ArcGIS^{TM} and based on the United States Geological Survey (USGS)-published global geologic map (Williams et al. 2011a). The Io database is a comprehensive digital source of the *Galileo* Io data and of several derived data products, and

includes definitions and mapping of geological units such as paterae, lava flows, mountains, plains, and plume deposits. Establishing geologic associations with the detected hot spots provides crucial information towards understanding Io's volcanism and geophysics.

In Section 2, we describe our analysis methodology, including photometry, single-temperature blackbody fits, image navigation, geologic associations and spatial statistics. Beginning in Section 3, we provide a general summary of the data obtained between 2001 and 2016 and focus on the temporal variations in hot spot detections and calculate the total Lp-band (3.8 μm) intensity and power output from hot spots from each period of observation. We also investigate the spatial distributions and geologic associations of the detected hot spots, which include calculation of the global power output from hot spots as a function of both longitude and latitude. In Section 4, we compare the hot spot activity with the activity observed during the *Galileo* mission. We also compare our observations with the heat flow distribution predicted by current tidal heat dissipation models. Section 5 presents a summary of our conclusions.

3 Observations and Analysis Methods

3.1 Observations

The data used in our analysis were obtained between 2001 and 2016, with a total of 14 distinct datasets (Table 1). A dataset is loosely defined as a set of observations performed within the same year and in close succession, ideally providing full longitudinal coverage of Io. All observations are ground-based, using adaptive optics on the 10-m Keck II and 8-m Gemini North telescopes, where we use the NIRC2 and NIRI imagers respectively, with exception of *New Horizons* data provided in Tsang et al. (2014). Along with the data presented in Tsang et al. (2014), we also included data previously provided by Marchis et al., (2005), de Pater et al. (2014a), and de Kleer and de Pater (2016a;b) corresponding to observations performed in 2001, 2010, and 2013 2015, respectively. The rest of the observations taken in 2003, 2004, 2005, 2007, 2008, and 2009 have not been published in their entirety.

Various Near-IR filters were used, ranging from 1.02 μm to 4.67 μm, although only one eruption at Surt in 2001 (Marchis et al., 2002) was detected at wavelengths below the Kc-band filter centered at 2.27

μm. The narrow Kc-band (2.27 μm), broad Lp-band (3.78 μm), and broad Ms-band (4.67 μm) filters were used consistently in each dataset beginning in 2001. Beginning in 2011, the narrow-band H_2O, PAH, Br_α-continuum, and Br_α filters, corresponding to wavelengths of 3.06 μm, 3.29 μm, 3.99 μm, and 4.05 μm respectively, were also used consistently for the observations thereafter. Table 1 provides a summary of all datasets and Figure 1 shows several example images from 2011. Table 2 provides a summary of the filters used over the course of the program for the Keck and Gemini telescopes.

A distinction is made between the observations in 2001-2013 and those made in 2013-2016. Between 2001 and 2013 the observations of Io were sporadic and often occurred over just a handful of nights within a year. Table A1 in the Appendix lists all detections not previously published within this period. In contrast, between 2013 and 2016 a systematic, high-cadence program was implemented over 100 nights. The 2001-2013 observations can be viewed as a snapshot into yearly variability while the 2013-2016 observations provide a snapshot into daily to monthly variability.

3.2 Photometry and Detection Limits

We calculated the intensity of hot spots in each filter using aperture photometry, the methods of which are described in detail in de Pater et al. (2014a) and de Kleer and de Pater (2016a). On photometric nights, a standard star was used to flux calibrate the Io images. On non-photometric nights, Io's intensity was calibrated to the brightness of the disk, which is stable over time after correction for Io's geocentric and heliocentric distance. Foreshortening near the limb was corrected for by dividing the intensities by the cosine of the emission angle. Errors in the intensities were determined by adding a 15% photometric uncertainty in quadrature to the standard error of measured intensities at each aperture radius.

Ideally, we would find and measure the intensity of all active hot spots. However, many factors, including atmospheric conditions, the telescope and filter used, and foreshortening due to the hot spot locations near the limb at the time of observation, reduces the detection of all active hot spots to those that are bright enough to be above the detection limit of each filter. An analysis of these detection limits for the Keck and Gemini North data is presented in de Kleer and de Pater (2016a). The following equations are provided for Keck:

$$\text{Keck Lp: } F(\mu) > -17.7\mu + 10.9 \text{ [GW/}\mu\text{m/sr]} \quad (1)$$

$$\text{Keck Ms: } F(\mu) > -15.0\mu + 8.1 \text{ [GW/}\mu\text{m/sr]} \quad (2)$$

where μ is the cosine of the emission angle. These equations are valid for greater than 0.2 and flux densities greater than 1.5 GW/μm/sr for Keck. At values greater than roughly 0.5, the equations yield negative fluxes which can be interpreted as any eruption with a flux density greater than 1.5 GW/μm/sr will be detected. For faint sources and locations close to the limb these equations are no longer valid due to factors that include nearby hot spot contamination, brightness of disk background, and variations in data quality.

From these equations, we created longitudinal sensitivity maps for observations in the Lp-band and Ms-band at various intensities based on the central meridian longitude for each observation since 2001. The maps are displayed in Figure 2. Combining the Lp-band longitudinal sensitivity at 10 GW/μm /sr with a latitudinal bias determined by the surface area covered by 1 square degree at a given latitude, results in a map of the global relative sensitivity provided in Figure 3.

3.3 Temperature Fits

When a given hot spot was detected at two or more wavelengths, we estimated its temperature based on single-temperature (1-T) blackbody fits. To calculate the power output from the hot spots, we used the Stefan-Boltzmann equation, $P = A\sigma T^4$. T is the temperature and A is the area obtained through the fit, σ is the Stefan-Boltzmann constant (5.67×10^{-8} W/m^2/K^4), and we assume an emissivity of 1. To determine an error in the blackbody fits, we employed a method described in de Pater et al. (2014a) where the uncertainties in radiance at the shortest and longest wavelength are subtracted from the measured radiance of the shortest and added to the measured radiance of the longest wavelength, and vice versa, with a new blackbody fit derived in each case. In using this method, we encompass the range of model fits to the data based on the extreme errors in the shortest and longest wavelength data. An example of this method is given in Figure

4. The extreme errors were then divided by the $\sqrt{2}$ to obtain more representative uncertainty range. The uncertainties derived in this way agree with those derived from a full Markov Chain Monte Carlo method described in de Kleer and de Pater (2016a). There were 71 detected hot spots for which a blackbody fit was attainable on at least one date and 17 detected hot spots for which a reasonably constrained blackbody fit was not attainable for any date. Table A1 in Appendix A provides the 1-T temperatures for hot spot detections between 2001 and 2016 that were not published previously.

It is important to note that the power calculations from a 1-T fit are considerably lower than the actual total thermal emission from the hot spot in most cases given the wavelengths of the observations. Often, hot spots are at low enough activity levels (with the exception of outbursts) where the data are only on one slope of the blackbody curve, missing the peak wavelength of thermal emission. As a result, we are also viewing a restricted surface temperature range. The temperature derived from a 1-T fit can be viewed as the lower limit temperature of the hot spot because it represents the mean temperature of a hotter active center surrounded by cooling lava which exhibits a broad range of temperatures.

3.4 Locations and USGS Geodatabase

Hot spot positions were calculated by projecting the images onto a simple cylindrical projection of Io's surface. To do this, it was first necessary to determine the center of Io's disk in the image, the radius of disk, the sub-observer latitude and longitude and the north pole angle, at the time the image was taken. The ephemeris information was taken from the Jet Propulsion Laboratory Horizons database [ssd.jpl.nasa.gov/horizons.cgi]. With this knowledge, the image could be accurately projected with the greatest source of uncertainty arising from the error in finding the precise center of the disk, which contributed a 1° uncertainty. The resulting measured hot spot positions are given in West Longitude throughout this paper. An example of a map constructed from the new data is shown in Figure 5c, in comparison with previous maps from 2001 (Marchis et al., 2005) and 2010 (de Pater et al., 2014a).

The average position of each hot spot, along with its radiance and derived temperature, emission area, and energy output were input into the Io USGS database. From there, new hot spot classes were created based on similarities in geology and eruption style.

For geologic associations, we first went through each of the 88 hot spots and investigated the defined geologic units at and around the emission site. There are numerous sources of uncertainty in specifying an emission site. The spatial resolution of the images for the Gemini NIRI and Keck NIRC2 are typically around 80 km/pixel and 40 km/pixel at disk center, respectively. Given these resolutions, it is difficult to establish if a hot spot has multiple emission sites, if the emission site changes over the course of time, or if the emission site is extended over a broad region, as is the case with recently emplaced lava flows. Uncertainty also arises in specifying an exact location given the error in measurement from images (usually around 2-3°). With that said, we took the average position of each hot spot from the 14 observation periods and analyzed a region within the uncertainty range around the hot spot. Based on the average positions, we then associated each hot spot with geologic features, with the most attention given to patera features. The geologic interpretations for the patera, or volcanic depression, units obtained from Williams et al. (2011a) are summarized as follows. The units will be referred to throughout the paper.

Dark Patera Floor: Silicate lavas possibly mixed with sulfur flows or sulfurous pyroclastic material. The darker the surface the more likely it was recently emplaced. Possibly a coalesced silicate lava flow, crusted lava pond, or lava lake.

Bright Patera Floor: Lava flows, ponded flows, or lava lakes with high sulfur content.

Undivided Patera Floor: Coalesced lava flows, crusted and ponded lava flows, or lava lakes of indeterminate composition. Units are older than bright or dark patera floor units.

3.5 Spatial Statistics

Spatial statistics were implemented to establish quantitative trends in the distribution of detected hot spots on Io. The mean pairwise distance and nearest neighbor methods were used to test for clustering, uniformity, or randomness in the distribution. These methods were developed from past methods used in Hamilton et al. (2013) and de Kleer and de Pater (2016b). The mean pairwise distance computes the mean distance of a volcanic center from each of the other volcanic centers and then calculates the mean of the mean to obtain a single distance for a given distribution. The nearest neighbor analysis measures the pairwise distance of a detected volcanic center with its closest neighbor and then calculates the mean of all pairwise

distances. Both methods use great-circle distances.

To implement these methods, we first had to establish a null hypothesis for each considering surface area biases. The null hypothesis was established by generating 10,000 realizations of N randomly distributed locations assuming an underlying continuous uniform distribution. The sampling was weighted by the area in each square degree as a function of latitude to preserve the area bias in the simulations. The lower the latitude, the more surface area and the more likely a sample would be chosen in that region. At the end of each of the 10,000 simulations the mean latitude, mean distance, and nearest neighbor distance were calculated. After all simulations were complete, the average of each of the methods over all simulations was determined and used as the null hypothesis.

In performing the nearest neighbor analysis, two test statistics R and c are defined as follows:

$$R = \frac{\overline{r_a}}{\overline{r_e}} \tag{3}$$

$$c = \frac{\overline{r_a} - \overline{r_e}}{\sigma} \tag{4}$$

In these equations, $\overline{r_a}$ and $\overline{r_e}$ represent the actual and expected mean pairwise nearest neighbor distances, respectively. The expected standard deviation of the nearest neighbor distance for a random distribution with N points and within an area A is calculated as:

$$\sigma = \frac{0.26136}{\sqrt{N^2/A}} \tag{5}$$

As stated and shown in Figure 4 in Hamilton et al. (2013), the ideal values and standard deviations of R and c vary depending on the sample size and region of interest. By comparing the ideal values of R and c and their standard deviations to the computed R and c using equations 3 and 4 for the hot spot pool, it is possible to establish statistically significant spatial distributions. If the actual value of R is more than $+2\sigma$ over the ideal value of R then the locations display spatial uniformity, and if the actual distance is more than -2σ under the expected distance, than the locations display clustering. However, c must also be outside its 2σ limits to make a spatial distribution claim with confidence. If R and c are both within the 2σ limits

than the null hypothesis cannot be rejected and if one is within its 2σ limits than the result is inconclusive.

We also calculated the mean absolute latitude for the data and the subsets we created. The null hypothesis of the mean absolute latitude calculated through the simulations for any sample size, N, was 32.7° with a 1° standard deviation of 2.4° for N=88. The mean absolute latitude obtained from the simulations is equivalent to the theoretical value of 32.7° expected for an area-weighted mean absolute latitude. The results of these three analyses will be presented when each subset is analyzed. The uncertainties provided with the results are 1° standard deviations.

4 Results

4.1 Inventory of hot spot detections

Over the course of the observations we identified 88 distinct hot spots. Of the 88 hot spots, 82 were detected multiple times, including three sites - Loki Patera, Janus Patera and Marduk Fluctus - that were detected every time the observation geometry permitted. We also detected 24 hot spots from which no thermal emission was detected by *Galileo* instruments, including Uta Patera and Chalybes Regio which were both observed consistently throughout the program. Uta Patera was detected by *Voyager* (hot spot 25) (McEwen et al. 1985), and there may have also been one poor quality detection in May of 2001 by *Galileo*, however, for a vast majority of the *Galileo* epoch, Uta was not detectable. Table A1 in Appendix A gives a list of all ground-based detections throughout the program, excluding those detected in 2001 which are provided in Marchis et al. (2005) and between 2013 2015 which are provided in de Kleer and de Pater (2016a). Figure 6 displays the average location of each hot spot along with defined geologic units within the USGS map.

Considering all detections, the mean absolute latitude was 30.0° indicating a slight tendency for hot spots to occur at lower latitudes given the null hypothesis mean absolute latitude for randomly-distributed hot spots of 32.7±2.4°. Of the 88 hot spots, only three had average positions above 60° latitude. However, extensive high-latitude lava flow fields suggest that there is currently active or recent (at least, recent enough for the flow fields to be still visible - Veeder et al., 2009) volcanic activity at these latitudes. It is difficult to

determine if the lack of detections above 60° can be attributed to the observation bias alone, or if there were only rare high-energy events at high latitude regions during our program, but the topic will be revisited in Section 4.1. We cannot reject the null hypothesis of a uniform random distribution with statistical significance based on the nearest neighbor or mean distance methods when considering the entire sphere. This result has been established by previous authors for the *Galileo* data (Lopes-Gautier et al., 1999; Hamilton et al., 2013).

With respect to the number of adaptive optics detections by hemisphere, there were 47 hot spots in the leading hemisphere, 41 in the trailing hemisphere, 43 in the antijovian hemisphere, 45 in the subjovian hemisphere, 48 in the southern hemisphere, and 40 in the northern hemisphere. Based on these numbers, and not considering the type of eruption, there does not appear to be any dominant trend in the concentration of detectable hot spots based on hemisphere, further confirming a random distribution of hot spots over the entire surface of Io.

4.2 Outbursts and Mini-Outbursts

Volcanic outbursts on Io represent the most powerful eruptions in the Solar System. They are defined as events that double the total 5.0 μm flux of Io during their short-lived eruption peaks (Blaney et al., 1995). However, because outbursts decay quickly, they do not have a large contribution to the total power output of Io over time (Davies, 2007; Veeder et al., 2012). Davies (2007) estimated the contribution of outbursts to be 1.7% of Io's total annual power output. Mini-outbursts are also powerful eruptions with similar eruption characteristics, but their peak 3.8 μm emission is a factor of $\sim$5 lower than outburst eruptions (de Kleer and de Pater, 2016a).

We identified five outburst and 15 mini-outburst eruptions from ground-based observations since 2001, which took place at 16 distinct locations on Io's surface. Each of these eruptions has been previously published individually but Table 3 provides a summary of all outbursts and mini-outbursts throughout the program. Figure 7 provides their locations. Outburst eruptions prior to 2001 are provided in Spencer and Schneider, (1996); Davies, (2007); and Veeder et al., (2012).

Only four of the 16 distinct outburst and mini-outburst sites were outside the trailing hemisphere. In

contrast, the number of large eruptions was comparable between the subjovian and antijovian hemisphere, with seven and eight distinct eruption sites, respectively. The mean absolute latitude of all outbursts and mini-outbursts is 37.5 which is within the 1 bounds of 32.7° which is within the 1σ bounds of 32.7±5.4° for N=16, while the mean absolute latitude for outbursts is 46.2°, significantly larger than the expected absolute latitude of 32.7±9.6° for N=5.

Pillan Patera, Kanehekili Fluctus, and Kurdalagon Patera had mini-outbursts detected multiple times. In the case of Pillan Patera and Kanehekili Fluctus, these sites have other similarities in that both are highly variable in their activity, both are approximately 400 km from mountainous regions that host persistent hot spots that are likely lava lakes: Janus Patera (de Pater et al., 2004; Davies et al., 2012) in the case of Kanehekili Fluctus, and Pele (Davies et al., 2001) in the case of Pillan Patera. For a comparison, the mean pairwise distance of all hot spots in our dataset (N=88) is approximately 2800 km and the nearest neighbor distance is 511±218 km. It is difficult to determine if these similarities have a physical significance in terms of the geophysics of their respective regions based on these observations alone. As of now, this speculative, potential connection between a persistently active volcanic center and a more variable volcanic center has not been observed at other locations. However, mini-outbursts that were detected close in time and location have been speculated to be related: de Pater et al., (2016a) suggested a shared magma source for the Tung Yo and Sui Jen Patera eruptions, and de Kleer and de Pater (2016a) suggested that a string of southern hemisphere eruptions could have resulted from each eruption triggering the next. While this has yet to be proven, it is possible that a similar triggering mechanism is at work behind these mini-outbursts events at Pillan Patera and Kanehekili Fluctus. This could potentially be a result of their proximity to mountain-forming regions and/or their proximity to persistently active volcanic centers.

4.3 Persistent Hot Spots

A persistent hot spot is defined as a volcanic center that was always active during the observing period. Between 2001 and 2013 there were ten such hot spots detected, i.e., ten different volcanic centers that were always active every time the observation geometry permitted us to observe that location. The higher temporal frequency observations in the 2013-2016 data expose short-term variability that could not be observed with

the yearly observations between 2001 and 2013. In de Kleer and de Pater (2016a), a persistent hot spot is defined as being consistently active for >1 year and being detected whenever the geometry was favorable during their period of activity. Twelve hot spots were included in this definition, seven of which were also persistent in the 2001-2013 dataset.

To overcome this ambiguity in the definition of "persistent", we defined a detection fraction as the number of detections of a hot spot over the number of times a hot spot was detectable given the viewing geometry. Taking only those hot spots with a detection fraction >50%, we find a subset of 18 hot spots that include all those defined as persistent in the 2001-2013 low cadence data and 2013-2016 high cadence data with the addition of Isum Patera, Malik Patera, and Kurdalagon Patera. Figure 8 provides a summary of location and names of these newly defined persistent hot spots. Lastly, through analysis of NIMS data, Lopes et al. and Davies et al. defined a persistent hot spot as one that was detected in every observation where geometry was favorable and the hot spot could be resolved from its neighbors. This definition is not used but it is important to keep in mind when comparing the Galileo datasets and its classifications with what is provided here.

With respect to hemispheres, 13 persistent hot spots out of 18 are in the antijovian hemisphere and 13 persistent hot spots are also in the leading hemisphere. The absolute mean latitude of all 18 persistent hot spots is 25.9° which is over a 1σ deviation from the expected $32.7\pm5.1°$ mean absolute latitude based on a random distribution (N=18) after accounting for biases. The significance of this distribution in relation to tidal heating models is discussed in Section 4.3.

A majority of the hot spots have a mean 1-T temperature between 500 K and 700 K. Loki Patera is the only persistent hot spot with a mean temperature below 450 K. This is because of Loki Patera's tremendous surface area (21,500 km^2 - Veeder et al., 2012) which is likely dominated most of the time by a passively cooling lava surface (Davies, 2003; Matson et al., 2006). Otherwise, the rest of the 1-T temperatures derived from the adaptive optics data are taken to be indicative of silicate volcanism. These results demonstrate the capability of ground-based, adaptive-optics observations to provide insights into eruption style which are in agreement with our current understanding of Io's volcanism based on spacecraft data.

4.4 Association of Hot Spots with Geologic Surface Features

Associating the detected hot spots with patera-type classifications in the global geologic map of Io (Williams et al., 2011a), we found 38.6% of the hot spots to be associated solely with dark paterae, and 62.5% having at least a dark patera component. Another 21.6% of hot spots were classified as undivided paterae, 3.4% of hot spots were classified as bright paterae, and 12.5% of hot spots were not associated with any patera feature. For comparison, Williams et al. (2011b) provided the distribution of geologic material units as a percentage of Io's surface and found that bright patera floors, dark patera floors, and undivided patera floors account for 0.41%, 0.51%, and 1.54%, respectively. Assuming the mean patera size is similar for each material, the surface area percentages correspond to 16%, 20%, and 62% of the total number of mapped patera for bright patera, dark patera, and undivided patera, respectively. Comparison of the percentages of total patera for each material type with the number of hot spots associated with patera of that material indicates a tendency for hot spots to be associated with dark patera. In contrast, there are relatively few bright patera hot spots given their total surface area is comparable to that of dark patera. Table 4 provides a summary of each hot spot detected and its patera association. Figure 9 shows the location and patera association of each hot spot.

Dark paterae are the dominant association, with 55 of the 88 hot spots having at least a dark patera component. This agrees with the *Galileo* epoch observations (Veeder et al., 2011; 2012; 2015). In this previous work, 193 dark patera were examined and thermal emission quantified, yielding a total thermal emission of 43 TW (Veeder et al, 2015). We note that many of these dark features were too small or too cool to be detected as thermal sources by ground-based telescopes. The spatial distribution of dark patera hot spots does not significantly deviate from the null hypothesis (i.e. uniform random distribution).

Figure 10 shows the locations of hot spots associated with solely undivided paterae and hot spots not associated with paterae. There are 19 solely undivided paterae and 39 paterae with an undivided component. The absolute latitude, mean distance and nearest neighbor analyses did not produce a significant deviation from the null hypothesis, but there is a tendency toward clustering. Of the 19 undivided paterae, 12 are within $\sim 3^\circ$ of a mountainous region or within $\sim$95 km as measured on a great circle. Because undivided paterae typically represent cooled silicate or currently inactive sites, it is likely that the 19 solely undivided

paterae established using *Voyager* and *Galileo* imagery are now dark or bright paterae due to their recent eruptions. These undivided classified hot spots are then interpreted as sites that were inactive during the *Voyager* and/or *Galileo* epoch.

Hot spots not associated with a patera correlate well with lava flows and/or mountainous regions. Of the 11 hot spots in this category, nine lie within *Galileo*-map lava flows, eight of which are primarily undivided flows although three have small dark flows near the determined emission site. For those that did not have a dark flow component during the *Galileo* epoch, we can expect that dark (silicate) flows have been emplaced at these emission sites since the *Galileo* mission. The two detected hot spots not associated with paterae or lava flows were less than 30 km from mountains. Another four hot spots associated with previously seen lava flows but not paterae are also within 30 km of mountains, hence one-half of the non-patera detections are near mountainous regions.

Of the 18 persistent hot spots, seven are associated with an undivided patera unit, while six are associated with a dark patera unit. The rest of the persistent hot spots are associated with paterae that have multiple unit types. While the fraction of persistent hot spots associated with dark paterae (33%) is therefore representative of the population of all hot spots (38.6% associated with dark paterae), the fraction of persistent hot spots associated with undivided patera ($\sim$40%) is nearly double that of the hot spot population as a whole (21.6%). In contrast, Williams et al. (2011b) found that 45.3% of hot spots detected by *Galileo* originated in dark paterae and only 18.6% from undivided patera units. For the seven hot spots associated with undivided paterae, their association suggests that they would have not been classified as persistent hot spots during the *Voyager* and/or *Galileo* epoch, and, in fact, would have been inactive during that period or were below the level of detection. As a result, these persistent hot spots, which have been a significant contribution to Io's global heat flux in the AO epoch (2001-2017), were once small or not-contributing to the heat flow for a time in the *Galileo* epoch (1996-2001). In other words, volcanic activity in these locations appears to be intermittent.

Figure 11 shows the locations of the persistent hot spots with respect to lava flows and mountainous regions. There is no evident correlation between persistent hot spots and these geologic features. Instead, the persistent hot spots display a wide range of characteristics based on these associations. Of the 18 persistent

hot spots, four do not exhibit lava flow units (i.e., Gish Bar Patera, Tawhaki Patera, Janus Patera, Pele), suggesting strong confinement of erupting lava, and five persistent hot spots are associated with dark lava flow units (i.e., Prometheus, Amirani, Masubi Fluctus, Isum Patera, Kurdalagon Patera) indicating ongoing lava emplacement at the time of *Galileo*. Another five are associated with older, undivided lava fields (i.e., Tupan Patera, Malik Patera, Marduk Fluctus, Uta Patera, Culann Patera). With respect to mountain features, eight persistent hot spots are near identified mountains or mountainous regions (i.e., Malik Patera, Gish Bar Patera, Zal Patera, Tawhaki Patera, Uta Patera, Pele, Marduk Fluctus, Culann Patera).

4.5 Global Intensity at 3.8 μm and Global Power Output

For each ground-based observation dataset we calculated the total Lp-band (3.8 μm) intensity and the total power emitted from the hot spots. Due to Loki Patera's high power output the results are shown both including and excluding Loki Patera. We also made the calculations excluding large brightening events if one was present in a dataset. Excluding Loki Patera and other large brightening events from the global Lp-band intensity and power output calculations helps in understanding the total contribution from lower energy but still detectable hot spots during an observation. The results are presented in Table 5.

For ground-based observation periods with full longitudinal coverage (N=8) there was a mean of 24 hot spots detected with a 1 standard deviation of 2 hot spots. The total Lp-band intensity from hot spots, not considering Loki Patera or any significant brightening event, remained relatively level with a mean of 64 GW/sr/μm with 1 standard deviation of 11 GW/sr/μm. Similarly, the total power output, not considering Loki Patera or any significant brightening event, remained relatively level with a mean of 2030$\pm$390 GW/sr/μm. While these values only represent hotpots that are detectable at the time of observation, they suggest the global and time-averaged heat flux from volcanic sites to remain relatively constant.

In addition to the global intensities at the Lp-band, Figure 12 provides the timelines of Lp-band intensities for individual hot spots. The monthly and/or yearly averages are also included for hot spots with a sufficient number of individual measurements over the timeline. A motivating factor in making these timelines was to investigate similarities in Lp-band intensity for hot spots within regions. In the case of Janus Patera,

Kanehekili Fluctus, and Uta Patera, the intensities for Janus Patera and Uta Patera were at low to moderate levels with respect to their timelines prior to and following Kanehekili Fluctus' significant brightening event in 2010. As noted previously, Janus Patera and Uta Patera also display an increase in intensity in 2013 followed by a level yearly average for 2014 and 2015. In the case of Pele and Pillan Patera, Pele brightened while Pillan Patera had significant brightening events in 2007, 2010 and 2015 although, there is a brightening event for Pele at the beginning of 2002 where Pillan Patera did not brighten. This possible linkage is considered in detail in Section 4.1.3. Lastly, Zal Patera and the hot spot within Chalybes Regio both exhibit sharp declines in Lp-band intensity followed by sharp increases at the start of both 2014 and 2015.

By comparing timelines of hot spots in similar regions, it may be possible to establish connections between hot spots or monitor changes in the global heat flow distribution. While the current timelines using just the detections from 2001-2016 do not have enough data points over a long enough time to establish clear trends or connections between hot spots, the features we just noted may become more prominent with a large sample size, and demonstrate the value of continued observation. However, this could already partially be achieved by combining *Voyager* and *Galileo* data with the timelines produced here. For example, an extended timeline of 3.8-m radiant intensity for Tupan Patera and Prometheus Patera is provided and discussed in Section 4.1.3. Similar timelines have also been produced for Janus Patera and Kanehekili Fluctus (de Pater et al., 2014a), Pele and Pillan Patera (de Pater et al., 2016b) and Loki Patera (de Pater et al., 2017).

4.6 Spatial Distribution of Hot Spots

4.6.1 Latitudinal Distribution of Temperature

The temperature of an eruption provides insight into the composition and potential origin of the magma. Considering both fluid and solid tidal heating that occur in separate layers and assuming significant magma mixing did not occur, Tyler et al. (2015) predicted that volcanoes at higher latitudes would typically have higher temperatures because their magma source is primarily generated from solid body tides in the deep interior. In contrast, volcanoes at lower latitudes would typically have lower temperatures because their magma source is generated from fluid body tides in the asthenosphere. Figure 13 shows the average 1-T temperature of all detected hot spots within 20° latitudinal bins. It also provides the average 1-T

temperature of the hot spot with the highest and lowest average temperature in each bin. The fact that higher latitude detections may be biased toward higher temperature eruptions due to the higher emission angle was addressed by plotting the average temperature and standard error per emission angle bin of 0.2 radians for hot spots under 30° latitude shown in Figure 14. There is a significant difference when comparing the average temperatures and standard error for the sample population under 30° absolute latitude to the average temperatures for all detections over latitude bins, for the same emission angle. For example, the mean emission angle for detections at latitudes above 50° absolute latitude (N=15) is 1.1 radians with a 1σ standard deviation of 0.1 radians and an average temperature of 682 K. Sampling from an emission angle above 1 radian for hot spots under 30° absolute latitude results in an average temperature of 492 K with a standard error of 61 K. The average temperature for detections above 50° absolute latitude is well outside of this range. The fact that the temperature remains relatively uniform over emission angle for detections under 30° absolute latitude demonstrates that the trend of higher latitude detections having higher temperatures cannot be accounted for by the observation bias.

In general, the average 1-T temperature of each bin increases with latitude as predicted by Tyler et al. (2015). There are local maxima between 10° and 30° latitude in the northern and southern hemispheres, a region that also exhibits an increased power output from hot spots as suggested by Figure 15 in the following section. The 1-T temperature of the minimum hot spot of each bin also displays an increase with respect to latitude while the 1-T temperature of the maximum hot spot peaks at 10° to 30° from the equator in each hemisphere.

4.6.2 Spatial Distribution of Power Output

The global power output from Io's volcanoes, and the distribution of volcanic thermal emission, have been extensively analyzed using primarily *Galileo* data by Veeder et al. (2012; 2015) and Davies et al. (2015). We perform a similar analysis to that of Veeder et al. whereby we sum the time-averaged power output of emission sites within 30° bins in the longitudinal direction and 20° bins in the latitudinal direction. However, our analysis is limited to those volcanic features that are hot enough and large enough to be thermally detectable by ground-based observations and have a reasonably constrained 1-T blackbody fit.

Veeder et al. (2012; 2015) also consider contributions from volcanic features that were not detected at thermal wavelengths by NIMS and PPR but were visible on the surface during the *Galileo* epoch, which we cannot do. As a result, the total time averaged power output we calculate from detectable hot spots of ∼23.8 TW is a factor of ∼2 less than the total power output provided in Veeder et al. (2015) of 56.2 TW. A comparison of the longitudinal distribution of detected hot spots and the power output is shown in Figure 15.

There are many similarities between the two power distributions, including peaks between 90°W to 120°W and 300°W to 330°W and a secondary peak between 210°W and 240°W. There is also very little activity at and around the subjovian point for both. This power output distribution is also seen in the high-cadence 2013-2015 dataset (de Kleer and de Pater 2016b). In our calculations, the peak at 90°W to 120°W is higher relative to the peak at 300°W to 330°W when excluding Loki Patera. This is due to the high activity of Kanehekili Fluctus (31.9°W, 17.4°S) and Janus Patera (37.5°W, 4.4°S), as well as Masubi Fluctus (56.2°W, 44.3°S) during the course of the program.

Figure 16 shows the latitudinal power distribution. The latitudinal power distribution is similar to the latitudinal distribution of detected hot spots. There is symmetry about the equator with peaks between absolute latitudes 10° and 30°, indicating greater heat flow near equatorial to mid-latitude regions rather than polar. The result does have an observation bias toward lower latitudes, thus the number of active hot spots and the power output from hot spots at higher latitudes may not be accurately represented in Figure 16, especially at latitudes greater than 60°. The $1/\cos(\theta)$ accounts for the larger area bias at lower latitudes. Scaling each bin by $1/\cos(\theta)$ acts to flatten the curve between 30° and 80° but the peaks for power output per area would still be between absolute latitudes 10° and 30°. Although, the higher latitudes show more power generation per unit area than the region between -10° and 10°. The relatively higher power output around 40°S compared to 40°N is attributed to the string of bright eruptions within close succession between 2013 and 2015 around 300°W. The decline in hot spot detections and power output at latitudes less than 10° from the equator correlates well with the purely asthenospheric solid body tidal heating model, which produces primary maxima at 30° north and south of the equator. This is further discussed in Section 4.3.

5 Discussion

5.1 Implications of the Geologic Associations of Hot Spots and Their Spatiotemporal Variability

It is difficult to establish clear trends in the temporal or spatial variability of hot spots and/or regions of hot spots based on ground-based observations thus far. However, our analyses indicate a steady global heat flux distribution over decadal timescales, with signs of an episodic behavior in hot spot activity in particular regions and a potential interconnectedness of the hot spots within these regions. The four primary pieces of evidence are as follows: (1) reactivation of once dormant, undivided patera; (2) presence of extensive, high-latitude and equatorial lava fields with no detected volcanic activity; (3) occasional similarities in the 3.8 μm intensity timelines for neighboring hot spots; and (4) the global distribution of active, dark patera features is consistent through *Galileo*'s and our observations. The following sections discuss the implications of each piece of evidence as they relate to this temporal and regional variation in volcanic activity.

5.1.1 Undivided Patera Associations

Geologic features that have been classified as undivided are interpreted as older, inactive units (Williams et al., 2011b). If a detected hot spot in our program is associated with an undivided patera feature, then its timeline of activity can be generalized as active prior to *Galileo*, dormant at some point during *Galileo*, and reactivating during our program. Of the 18 persistent hot spots, 7 or 38% were classified as solely undivided patera in comparison to the entire dataset where 22% were classified as solely undivided patera. Thus, there is a relatively high number of persistently active hot spots during our program that were recently inactive prior to the program. Moreover, because persistent hot spots within paterae have the largest volcanic contribution to Io's total surface heat flux, these undivided hot spots hint toward notable spatiotemporal variability in Io's heat flux. Figure 9 shows that undivided patera are commonly found in groups of two or three, often near mountainous regions. It is possible that the activity of these undivided patera groups is connected to mountain forming processes. Radebaugh et al. (2005) also pointed out a link between paterae and mountains when analyzing the *Galileo* dataset, where two or three paterae were commonly arranged

at opposite ends of mountains. They proposed that the arrangement potentially represents fractures that magma has intruded and lead to patera formation. If this is the case, then mountain forming processes have a significant effect on Io's surface heat flux and its temporal variations based on our classifications of these undivided, persistent hot spots near mountainous regions.

5.1.2 Distribution of Lava Flow Fields

There are three regions on Io's surface that have extensive lava flow fields but little detected volcanic activity during our program. The two equatorial regions are between 100°W to 140°W and 310°W to 20°W. The high, Northern latitude region is between 90°W to 250°W. The fact that there are extensive lava flow fields in these regions indicates significant volcanic activity, either ongoing or in the geologically-recent past. One potential reason for not detecting activity in these regions is that the activity is below our detection limit. If this were the case, then continuous lava emplacement could have occurred during our program at low-energy levels. This is more likely in the Northern latitude region where our detection limit is high and where the lava fields are classified as bright which typically represents lower temperature, possibly sulfur volcanism. For the equatorial regions, it is more likely that the regions were simply inactive. The classification of the lava fields in these regions as undivided supports this conclusion and leads to the interpretation that once active and extensive regions went dormant for at least a 20-year period.

5.1.3 Intensity Timelines at 3.8 μm

As discussed in Section 3.3, a motivating factor behind the timelines in Figure 12 was to investigate similarities in Lp-band intensity for hot spots within close proximity. Similarities in neighboring hot spot activity could result from a shared magma source along a fracture or a triggering mechanism after an eruption occurs. The Pillan Patera/Pele and Kanehekili Fluctus/Janus Patera pairs were used as examples for a potential triggering mechanism as Kanehekili Fluctus and Pillan Patera both exhibit highly variable activity with at least two mini-outburst class eruptions each over the program, while Pele and Janus Patera are identified as lava lakes (Davies et al., 2001; de Pater et al., 2004; Davies et al., 2012) with steady activity. In the case of Janus Patera and Kanehekili Fluctus, there are initial signs of a connection proposed in de Pater et al., (2014a). It is evident that after the large Kanehekili eruption, the activity at both Kanehekili

Fluctus and Janus Patera were at low levels for a period in time. Eventually, the activity of Janus Patera increased while Kanehekili Fluctus has remained at low levels. The behavior of these timelines may suggest a sharing of a magma source that was evacuated by the Kanehekili eruption and is now being recharged. In the case of Pele and Pillan, Pele brightened when Pillan had significant brightening events in 2007, 2010 and 2015 and both hot spots had low detected activity between 2010 and 2015. Pele and Pillan Patera are also located within 75 km of mountainous regions (the null hypothesis for a random uniform distribution considering 88 hot spots and 275 mountain units produces a nearest neighbor distance of 218±45 km), which may indicate a link between the two through mountain-forming processes that result in changing stresses in the lithosphere, which in turn affect magma supply. In potential contrast to this speculation based entirely on ground-based data, it is important to mention that during the *Galileo* epoch, in 1997, there was a massive outburst eruption emanating from a rift associated with the mountains to the North of Pillan Patera during which Pele's activity remained at its typical, constant behavior (Davies et al., 2001). The Chalybes Regio hot spot and Zal Patera form another neighboring pair of volcanoes that are located against mountains (within 10 km for Zal) with similarities in their timelines of activity. Both exhibit sharp declines in Lp-band intensity followed by sharp increases at the start of both 2014 and 2015. Although not conclusive evidence, these timelines are suggestive of links between neighboring hot spots, and as a result, regional temporal variations in heat flux. Further work will expand on these timelines by combining the *Voyager* and *Galileo* data with ground-based observations, looking at both the 3.8 μm intensity evolution and total thermal emission evolution of individual hot spots. Examples of extended timelines for Tupan Patera [Davies and Ennis, 2011] and Prometheus [Davies et al., 2006] are shown in Figure 18. For those hot spots that have been consistently active since the *Voyager* mission, these timelines of activity will provide close to 30 years' worth of data from which the temporal behavior of volcanism on both an individual and regional scale can be further investigated. For examples of the potential of such work for Loki Patera, see e.g., de Pater et al. (2017), and de Kleer & de Pater (2017).

5.1.4 Distribution of Thermally Detected Dark Patarae

While the previous paragraphs have discussed the spatial and temporal variations on a regional scale, analyzing the distribution of detected, dark patera hot spots, provides insights into the global surface heat flux distribution. Dark paterae are the most common volcanic features on Io and have the greatest contribution to Io's surface heat flux (Veeder et al., 2012;2015). We found that 38.6% of our detections were from regions with solely dark paterae and 62.5% had a dark patera component. Williams et al. (2011b) found that 45.3% of the *Galileo* thermal detections were associated with dark paterae but the total surface area of dark paterae was only 20% of the total surface area of all paterae, indicating a tendency for hot spots to be associated dark patera. The global spatial distribution of dark paterae was determined to be random for both our dataset and *Galileo*'s (Hamilton et al., 2013). With that said, the global distribution of active, dark patera features on Io has remained consistent between the *Galileo* observations and our observations. Thus, while there is indication of temporal variability in Io's surface heat flux on a regional scale, the global distribution in the surface heat flux has remained relatively constant over timescales comparable to the length of the *Galileo* mission (5.5-year period) and our program (15-year period). The following two sections further explore this topic.

5.2 *Galileo* Comparison

The *Galileo* NIMS data were generally obtained at a higher temporal and spectral resolution than the ground-based observations early in our program. Coverage of Io by NIMS was not consistent by longitude, generally with fewer observations of poorer spatial resolution obtained on the sub-jovian hemisphere. As a result, some AO observations collect better thermal emission data of some areas (such as Janus Patera and Kanahekili Fluctus) which had poor *Galileo* coverage. Many of the *Galileo* datasets had a much higher spatial resolution than possible from Earth. As a result, the number of distinct thermal sources detected primarily from *Galileo* data is 250 compared to the 88 in our dataset (Veeder et al., 2009, 2011, 2012, 2015). This number of 250 includes eight outburst eruptions, and small dark paterae with low enough thermal emissions to go undetected in NIMS data and by ground-based instruments. The fraction of hot spots outside of patera floor units in the *Galileo* NIMS dataset is approximately one-third (Williams et al. 2011b), while in

our dataset it is closer to one-seventh. This suggests that we are missing more hot spots outside of patera units than within patera units compared to *Galileo*. These hot spots are mostly cooling lava flows whose emission falls below our detection limit. It has been established that the heat flow from paterae provides the greatest contribution to Io's surface heat flux (Veeder et al., 2012; 2015). With that said, our ground-based observation bias toward the brighter eruptions does not hinder our ability to still establish regions with the most volcanic activity and does not appreciably limit the investigation into the global heat flux based on our detections. This is evident in Figure 15 in Section 4.3 which shows that the longitudinal heat flux from our program closely resembles the heat flux determined by *Galileo* observations. This suggests that over a 20-year span, the global heat flux distribution has remained relatively constant. Our findings from Table 5, displaying the total 3.8 μm intensity and power output from detected hot spots at each observation period, further establishes a consistent global heat flux through time, especially when not considering Loki Patera, which exhibited significant periodic variations in activity over this time (e.g., de Pater et al. 2017; de Kleer and de Pater, 2017). This is not to say that regional and/or short timescale variability does not occur. However, over decadal timescales that match that of the beginning of the *Galileo* mission to the end of our program, the overall global heat flux has remained steady in both magnitude and distribution.

While there were nearly 100 hot spots detected by *Galileo* that we did not detect, there were 24 hot spots that we detected that were not thermally detected by *Galileo*. Figure 17 displays the locations of these hot spots. Most, but not all, of these hotpots are located between 320°W and 40°W, a region where NIMS had poor coverage. The most notable hot spots not detected by *Galileo* are Uta Patera (34.8°S, 21.9°W) and the hot spot in Chalybes Regio (55.1°N, 68.1°W), which were consistently active throughout our program. It was mentioned in Section 3.1 that Uta Patera may have been detected once by *Galileo*. Similarly, Geissler et al. (2004) mentioned "a massive plume deposit that appeared and then disappeared during the *Galileo* mission, centered around 80°N, 100°W" and "in a poorly imaged region". Given the high uncertainties in position at high latitudes it is possible that the Chalybes Regio hot spot detected recently may have also been responsible for the plume deposit mentioned in Geissler et al. (2004). This would indicate that the Chalybes Regio hot spot had been sporadically active during *Galileo* and is a plume source. However, because the source of the plume deposit was not observed by *Galileo* and because of the large distance

between the Chalybes Regio hot spot we detected and the center of the plume deposit, we have classified the Chalybes Regio hot spot as not detected by *Galileo*. The rest of the hot spots not detected by *Galileo* were only detected a handful of times in the ground campaign.

As noted in Section 4.1.4, 38.6% of all our detections were associated with dark paterae and 21.6% were associated with undivided paterae. Of the hot spots detected by *Galileo*, 45.3% were associated with dark paterae and 18.6% were associated with undivided paterae. In general, the overall distribution of detected hot spots in our dataset and the relative quantities of the patera types associated with these hot spots mirrors the detections by *Galileo*.

Combining the *Galileo* and ground-based datasets to investigate the temporal behaviors of individual hot spots and regions will be the focus of future work. Figure 18 provides an example of 3.8 μm intensity evolution and the corresponding effusive rates based on estimates in Davies and Ennis (2011) for Tupan Patera and Prometheus Patera. Thermal emission data from both sites have been analyzed by Davies et al., (2006) and Davies and Ennis (2011), primarily through the *Galileo* NIMS dataset. The analyses suggest that both persistent volcanoes appear to be supplied from shallow magma chambers, with an episodic behavior similar to that of the terrestrial volcano, Kilauea. However, after the *Galileo* epoch and the increase in effusive activity at Tupan Patera in 2003, the activity at both sites, detected by ground-based observations, appears to decrease and remain relatively constant. For Tupan Patera, the radiances after 2003 at 4.7 μm are still within one standard deviation of the average provided in Davies and Ennis (2011). Persistently active volcanoes on Io and Earth can be highly variable in thermal emission (Davies and Ennis, 2011), and so the lower radiance detections after 2003 may not result from a significant change in volcanic behavior at these sites. Unfortunately, the large gaps in the ground-based timeline make it difficult to conclude if the activity at these sites is on the decline. Eruption peaks may have been missed between 2001 and 2016 and more frequent observations are likely necessary to truly establish the current behavior at many of the hot spots on Io.

5.3 Comparison with Tidal Heating Models

Comparison of our observations to current tidal heating models supports many of the conclusions previously established (Hamilton et al., 2013; Veeder et al. 2015; Davies et al., 2015). In general, our observations favor heat dissipation primarily in the asthenosphere causing greater surface heat flux at lower to mid-latitudes. According to solid body heating model end members the primary heat flow maxima occur 30° north and south of the subjovian (0°W, 0°N) and antijovian (180°W, 0°N) points and secondary maxima occur on the equator at 90°W and 270°W. As with previous analyses (cited above) of primarily spacecraft data, our observations show these maxima to be offset. This is evident in Figure 19, which plots the persistent hot spots in our program over the deep mantle and asthenosphere tidal heating end-member models (Hamilton et al., 2013). Based on Figure 15, our observations show primary maxima to be around 90°W-120°W and 300°W-330°W and a secondary maximum between 210°W-240°W. However, Figure 16 demonstrates that latitudinal heat flux from our observations, with primary maxima near ±30°, is in close agreement with the asthenospheric solid body tidal heating end member model.

From a longitudinal perspective, our findings are in better agreement with a model that considers both solid and fluid tidal heating as described in Tyler et al. (2015). This model produces primary maxima at approximately 90°W and 270°W. Our observations show close agreement to the model in the leading hemisphere but not in the trailing. In fact, observations in the trailing hemisphere show little resemblance to the model, as also pointed out in de Kleer and de Pater (2016b). It is important to keep in mind that the figures provided in Tyler et al. (2015) are only a few realizations from a large parameter space. While the model realizations considering fluid tidal heating do display hemispheric asymmetry, the asymmetry does not accurately depict the hemispheric asymmetry of persistent hot spots seen in the observations. Fluid tidal heating may help to explain Io's global pattern of volcanism, but the combination of fluid and solid body tidal heating as shown in Figure 6 of Tyler et al. (2015) could be improved by refining how these two processes optimally combine to minimize the residual between the model's predictions and observational constraints.

While our observations show the greatest heat flux from low to mid-latitudes, they also suggest a significant magma source feeding higher latitude regions. As pointed out in Section 3.1.1, outburst events had a

mean absolute latitude of 46.2°, with Tvashtar Patera being the highest in latitude at ∼61°N. The Chalybes Regio hot spot at approximately 55°N is surrounded by extensive lava flows and was consistently active during the program. It is also noted by de Kleer and de Pater (2016a;b) that there were numerous bright hot spots in a southern hemisphere region at latitudes between 40°S and 65°S in the years 2013-2015. Together, these observations indicate that heat dissipation is also occurring at depths beyond the asthenosphere and more likely in the mantle. This would also match our findings in Section 6.1 where the average hot spot temperature per bin increases with absolute latitude, potentially as a result of a larger component of mantle magma reaching the surface as latitude increases.

Figure 20 provides a 2-D representation of the global heat flux based on our hot spot detections. The orange and red hot spots are those that were most active during our program, typically providing the largest contribution to Io's total heat flux. Their size is determined on a log scale of their time-average power output over the course of our program. The distribution of the regions of highest heat flow from detected hot spots closely resembles the recent map of Io's volcanic heat flow in Davies et al. (2015).

6 Conclusions

We present a summary of Io's volcanic activity based on a compilation of ground-based observations, including the high-cadence program presented in de Kleer and de Pater (2016a;b). Our analysis includes 14 distinct observation periods gathered over the course of 15 years in which 88 individual hot spot sites were detected. Table A1 in the appendix summarizes the detections made between 2003-2015 that are published here in their entirety for the first time, and Figure 12 provides 3.8 μm intensity timelines for notable hot spots over the full course of the program.

We associate hot spots with geologic features, including patera type and proximity to mountains and lava flows, using the ArcGIS^{TM} USGS-published global geologic map (Williams et al. 2011a). Hot spots were most commonly associated with dark patera features (38.6% were solely dark patera and 62.5% had a dark patera component), interpreted as recently emplaced silicate lavas, a confirmation of previous analyses by Veeder et al., (2012; 2015). The spatial distribution using nearest neighbor and mean absolute latitude of the dark patera sites, as well as the distribution of all hot spots, was found to be random, a result that is

in line with previous findings from the *Galileo* dataset (Hamilton et al., 2013). Another 21.6% of hot spots were associated with undivided paterae, 3.4% of hot spots were associated with a bright patera, and 12.5% of hot spots were not associated with any patera feature.

Based on our classification and interpretation of undivided paterae and their proximity to mountainous regions, along with the distribution of extensive lava fields in relation to detected activity, there are signs of significant regional variations in the global heat flux distribution on monthly to yearly timescales. Overall, the global heat flux distribution remained relatively constant over timescales comparable to the span of the Galileo mission (5.5 years) and our program (∼15-years to date).

Comparing the location and activity of hot spot sites to tidal heat dissipation models confirms previous findings in that the heat dissipation appears to be primarily concentrated in the asthenosphere, resulting in a high time-averaged surface heat flux at low latitudes. However, in agreement with previous findings (Veeder et al., 2012; 2015), significant spatial deviations do exist from the asthenosphere heat dissipation model, suggesting a deeper source of magma ascent to be present as well. Evidence for a heat dissipation in the deep mantle includes outburst events with a mean absolute latitude of 46.2°, significantly higher than the expected average based upon a random distribution of hot spots of 32.7±9.6°. Also, the hot spot in Chalybes Regio, at approximately 55 N, is surrounded by extensive lava flows and was consistently active during the program. The persistence of this hot spot and the emplacement of extensive lava flows confirms the presence of a voluminous source of magma.

In many ways, therefore, the heat flux analyses presented here confirm findings that had been established before through extensive investigation of the *Galileo* and prior ground-based data. This is an important conclusion in itself because it provides confidence in ground-observations to extend the timeline of Io's volcanism and establish clear trends in the spatial and temporal variations in the surface heat flux which will further help to constrain heat dissipation models and our understanding of the interior mechanisms driving the extensive volcanism we observe. Future work will analyze the temporal activity and investigate the magma supply for individual hot spots and their respective regions by combining the continued ground-based observations of Io with spacecraft derived data.

7 Acknowledgements

The data presented in this paper were obtained at the W.M. Keck Observatories. The Keck Telescopes are operated as a scientific partnership among the California Institute of Technology, the University of California and the National Aeronautics and Space Administration. The Observatory was made possible by the generous financial support of the W.M. Keck Foundation. Our research was supported by the National Science Foundation, NSF grant AST-1313485 to UC Berkeley. Ashley Davies thanks also the NASA Outer Planets Research and Planetary Geology and Geophysics Programs for support. The authors recognize and acknowledge the very significant cultural role and reverence that the summit of Maunakea has always had within the indigenous Hawaiian community. We are most fortunate to have the opportunity to conduct observations of Ionian volcanoes from this Hawaiian volcano.

8 Appendix A

Table A1 lists all detections obtained with the Keck Observatory between 2003 and 2016, excluding those published by de Kleer and de Pater (2016a; b).

9 References

Belton, M. J. S., et al., 1992. The *Galileo* Solid-State Imaging experiment. Space Science Reviews. 60, 413-455.

Blaney, D.L., Johnson, T.V., Matson, D.L., Veeder, G.J., 1995. Volcanic eruptions on Io: Heat ?ow, resurfacing, and lava composition. Icarus 113, 220-225.

Carlson, R. W., Weissman, P. R., Smythe, W. D., Mahoney, J. C., 1992. Near-Infrared Mapping Spectrometer experiment on *Galileo*. Space Science Reviews. 60, 457-502.

Davies, A. G., L. P. Keszthelyi, D. A. Williams, C. B. Phillips, A. S. McEwen, R. M. C. Lopes, W. D. Smythe, L. W. Kamp, L. A. Soderblom, and R. W. Carlson, Thermal signature, eruption style, and eruption evolution at Pele and Pillan on Io, J. Geophys. Res. 106, 33,079-33,104, 2001.

Davies, A.G. et al., 2006. The heartbeat of the volcano: The discovery of episodic activity at Prometheus

on Io. Icarus 184, 460-477.

Davies, A.G. Volcanism on Io: A Comparison with Earth, Cam. Univ. Press, 2007.

Davies, A.G. and Ennis, M.E., 2011. The variability of volcanic activity at Zamama, Culann, and Tupan Patera on Io as seen by the *Galileo* Near Infrared Mapping Spectrometer. Icarus 215, 401-416.

Davies et al., 2012. Charting thermal emission variability at Pele, Janus Patera and Kanehekili Fluctus with the *Galileo* NIMS Io Thermal Emission Database (NITED). Icarus 221, 466-470.

Davies, A.G., Veeder, G.J., Matson, D.L., Johnson, T.V., 2015. Map of Io's volcanic heat flow. Icarus 262, 67-78.

de Kleer, K. et al., 2014. Near-infrared monitoring of Io and detection of a violent outburst Gemini eruption. Icarus 242, 352-364.

de Kleer, K. & de Pater, I., 2016a. Time Variability of Io's volcanic activity from near-IR adaptive optics observations on 100 nights in 2013-2015. Icarus 280, 378-404.

de Kleer, K. & de Pater, I., 2016b. Spatial Distribution of Io's volcanic activity from near-IR adaptive optics observations on 100 nights in 2013-2015. Icarus 280, 405-414.

de Kleer, K. & de Pater, I., 2017. Io's Loki Patera: Modeling of three brightening events in 2013-2016. Icarus 289, 181-198.

de Pater, I. et al., 2014a. Global near-IR maps from Gemini-N and Keck in 2010, with a special focus on Janus Patera and Kanehekili Fluctus. Icarus 242, 379-395.

de Pater, I. et al., 2014b. Two new, rare, high-effusion outburst eruptions at Rarog and Heno Paterae on Io. Icarus 242, 365-378.

de Pater, I. et al., 2016a. Keck Observations of Eruptions on Io in 2003-2005. Icarus 274, 284-296.

de Pater, I. et al., 2016b. Io: Eruptions at Pillan, and the time evolution of Pele and Pillan from 1996 to 2015. Icarus 264. 198-212.

de Pater, I. et al., 2017. Three decades of Loki Patera observations. Icarus 297, 265-281.

Hamilton, C.W. et al., 2013. Spatial distribution of volcanoes on Io: Implications for tidal heating and magma ascent. Earth Planet Sci. Lett. 361, 272-286.

Laver, C., de Pater, I., Marchis, F., 2007. Tvashtar awakening detected in April 2006 with OSIRIS at

the W.M. Keck Observatory. Icarus 191, 749-754.

Leone, G. et al., 2006. Volcanic history, geologic analysis and map of the Prometheus Patera region on Io. J. Volcanol. and Geotherm. Res. 187, 93-105.

Lopes-Gautier et al., 1999. Active Volcanism on Io: Global Distribution and Variations in Activity. Icarus 140, 243-264.

Marchis, F. et al., 2002. High-resolution Keck adaptive optics imaging of violent activity on Io. Icarus 160, 124-131.

Marchis et al., 2005. Keck AO survey of Io global volcanic activity between 2 and 5 microns. Icarus 176, 96-122.

Matson, D., Ransford, G.A., Johnson, T.V., 1981. Heat flow from Io. J. Geophys. Res. 86, 1664-1672.

Peale, S. J., Cassen, P., Reynolds, R. T., 1979. Melting of Io by tidal dissipation. Science. 203, 892-894.

Radebaugh, J., 2005. Formation and Evolution of Paterae on Jupiter's Moon Io. Thesis, Univ. Arizona, Tucson.

Russell, E., et al., 1992. *Galileo* Photopolarimeter/Radiometer experiment. Space Science Reviews 60, 531-563.

Smith et al., 1979. The Jupiter system through the eyes of *Voyager* 1. Science 204, 951-972.

Spencer and Schneider, 1996. Io on the eve of the Galileo mission. Annual Review of Earth and Planetary Sciences 24, 125-190.

Tsang, C.C., Rathbun, J.A., Spencer, J.R., et al., 2014. Io's hot spots in the near-infrared detected by LEISA during the New Horizons flyby. J. Geophys. Res. 119, 2222-2238.

Tyler, R.H., Henning, W.G., Hamilton, C.W., 2015. Tidal heating in a magma ocean within Jupiter's moon Io. Astrophys. J. Supp. 218-222.

Veeder, G.J., Matson, D.L., Johnson, T.V., Blaney, D.L., and Goguen, J.D., 1994. Io's heat flow from infrared radiometry: 1983 1993. J. Geophys. Res. 99, 17095-17162.

Veeder, G.J., Davies, A.G., Matson, D.L., Johnson, T.V., Williams, D.A. and Radebaugh, J., 2012. Io: Volcanic thermal sources and global heat flow. Icarus 219, 701-722.

Veeder, G.J., et al., 2015. Io: Heat flow from small volcanic features. Icarus 245, 379-410.

Williams, D.A. et al., 2011a. Geologic map of Io, USGS Scientific Investigations Map 3168, scale 1:15,000,000.

Williams, D.A., Keszthelyi, L.P., Crown, D.A., 2011b. Volcanism on Io: New insights from global geologic mapping. Icarus 214, 91-112.

10 Figure Captions

Fig. 1: Images of Io in November of 2011 taken by the 10-m W.M. Keck II telescope using adaptive optics at the wavelengths of 2.3, 3.8 and 4.7 μm. A majority of the thermal activity in the 2011 observation period was detected at wavelengths around 4 μm or longer with temperatures representative of primarily silicate volcanism. The central meridian longitude for Nov. 10, Nov. 11, and Nov. 12 ranged from 334°W-343°W, 194°W-195°W and 40°W-42°W, respectively, for the images shown. These images, along with the rest of the 2011 dataset, have not been published previously. In these images, Io North is up.

Fig. 2: Global maps displaying the relative sensitivity of the observations over Io's surface at various hot spot intensities with the Keck Lp-band and Ms-band filters during the entire program between 2001 and 2016. These maps are based on the equations provided in de Kleer and de Pater (2016b) for the detection limits of Keck using the central meridian longitude at the time of observation.

Fig. 3: Map of the relative sensitivity of the Keck observations between 2001 and 2016 at 10 GW/μm/sr including both the longitudinal sensitivity based on the central meridian longitude and the latitudinal bias determined by the decreasing surface area covered by 1 square degree as latitude increases. Hot spots are more likely to be detected near the equatorial regions and rarely at latitudes above 60° because of this bias. Yellow indicates regions with the highest probability of detecting an eruption with an intensity equal to or greater than 10 GW/μm/sr while blue represents regions where detecting an eruption of 10 GW/μm/sr is unlikely.

Fig. 4: A single temperature blackbody fit (black curve), with the high and low fit (red and blue dashed

curves) described in Section 2.3, of Amirani Patera in July of 2009 results in a temperature of 382±33 K over an area of 124±30 km^2. The single temperature blackbody fit for Loki Patera in November of 2011 results in a temperature of 476±22 K over an emission area of 175±42 km^2. Notice that all data points are on the positive sloping side of the curve which results in large uncertainties. To better constrain this blackbody fit, it would be ideal to obtain measurements at wavelengths between 5-10 μm.

Fig. 5: Global, projected maps of Io for observations in 2001 (from Marchis et al. 2005), 2010 (from de Pater et al. 2014a) and 2011. The maps are created by mosaicking images that are ideally observed at every 45° in longitude, or more frequently. In 2011, only 4 observations were made, limiting the span of the global map. The images are scaled to optimally present surface brightness contrasts.

Fig. 6: Map of the locations of all 88 hot spots detected during the program along with defined lava flow and diffuse deposit units in the ArcGIS^{TM} version of the USGS-published global geologic map (Williams et al. 2011a) using Galileo and Voyager imagery. Notice the equatorial regions between 100°W-140°W and 50°E-20°W in the maps coordinate system with extensive, primarily undivided lava fields with no hot spot detections. In West Longitude, these regions correspond to 100°W-140°W and 310°W-20°W, respectively. Also, notice the lack of hot spot detections at latitudes greater than 60°.

Fig. 7: Map of the outbursts and mini-outbursts detected over the course of the program. The size of the circle represents the power output on a logarithmic scale of the eruption, or largest eruption in the case of sites with multiple eruptions. Of the 15 distinct sites, 11 are in the trailing hemisphere.

Fig. 8: Map of the location and names of hot spots defined as persistent based on a detection fraction, defined as the number of detections of a hot spot over the number of times a hot spot was geometrically detectable, greater than 50%.

Fig. 9: Map of all detected hot spots and their patera associations. The spatial distribution of the patera

classes did not result in a statistically significant distribution. However, a visual scan of this map shows two large regions between 60°W-100°W and 80°E-30°E where nearly all hot spots are associated with dark patera. In West Longitude, these regions correspond to 60°W-100°W and 280°W-330°W, respectively.

Fig. 10: Map of the hot spots associated with undivided paterae and those not associated with a patera. Both classifications are frequently found near mountainous regions, and in the case of undivided patera, there are often two or three hot spots near a mountainous region.

Fig 11: Map of the locations of persistent hot spots with geologic features. Persistent hot spots display a wide range of characteristics when associated with geologic features in the Io USGS map. See Section 3.2.

Fig. 12: Timelines of 3.8 μm intensity of notable hot spots over the course of the observing program between 2001-2016. For hot spots with a high frequency of detections, especially between 2013-2016, the monthly and/or yearly averages of the 3.8 μm detections are also included.

Fig. 13: A profile of the average temperature of all detections within 20° bins, along with the highest and lowest average temperature hot spot in each bin based on 1-T blackbody fits.

Fig. 14: Plot of average temperature and standard error per emission angle bin of 0.2 radians for detections under 30° absolute latitude.

Fig. 15: The total calculated time-averaged power output for all hot spots detected between 2001-2016 within longitudinal bins of 30° compared to the longitudinal power output determined from Galileo data (Veeder et al. 2012;2015). The two profiles show strong similarities with the exception that the 2001-2016 power output is approximately a factor of two less than the *Galileo*. See Section 3.4.2 for further discussion of these profiles.

Fig 16: The total calculated time-averaged power output for all hot spots detected between 2001-2016 within latitudinal bins of 20°. The $1/\cos(\theta)$ curve is provided to show the scaling factor that would account for less surface in the higher latitudes. The maxima seen between latitudes of 10° and 30°N and 10° and 30°S in each hemisphere with a decline in power output at higher latitudes, is in agreement with an asthenospheric solid body end member heating model (Veeder et al., 2012; Hamilton et al., 2013; Davies et al., 2015).

Fig 17: Map of the locations of hot spots detected in the program between 2001-2016 that were and were not detected by *Galileo*. Many of the hot spots not detected by *Galileo* are between 320°W and 40°W, a region that NIMS had poor coverage.

Fig 18: Timeline of the 3.8 *mu*m intensity at Prometheus Patera and Tupan Patera combining *Galileo* NIMS and ground-based observations and including estimates on effusive rate established in Davies et al. (2006) and Davies and Ennis (2011). The dotted lines are to help guide the eye. For both hot spots, activity apparently drops to a low, constant level after a period of enhanced thermal emission and increased effusion rate. These observations may be a result of a larger eruption causing a longer recharge time of the magma source.

Fig 19: Map of defined persistent hot spots in the program plotted over the solid body tidal heating end-member models generated by Hamilton et al., (2013). The asthenosphere heating model is in better agreement, especially when considering a 30° shift to the West (see also Veeder et al., 2012) which is shown to be possible when considering a partial fluid layer (Tyler et al., 2015). However, significant discrepancies still exist between observations and model outputs.

Fig 20: The map displays the frequency of detections of a hot spot and its relative time-averaged power output for all hot spots detected over the program. The color represents the frequency of detections with red being highly active and dark blue being rarely active above the detection limit. The size of the circle represents the contribution of the hot spot to the total power output on a log scale.

Figure 1:

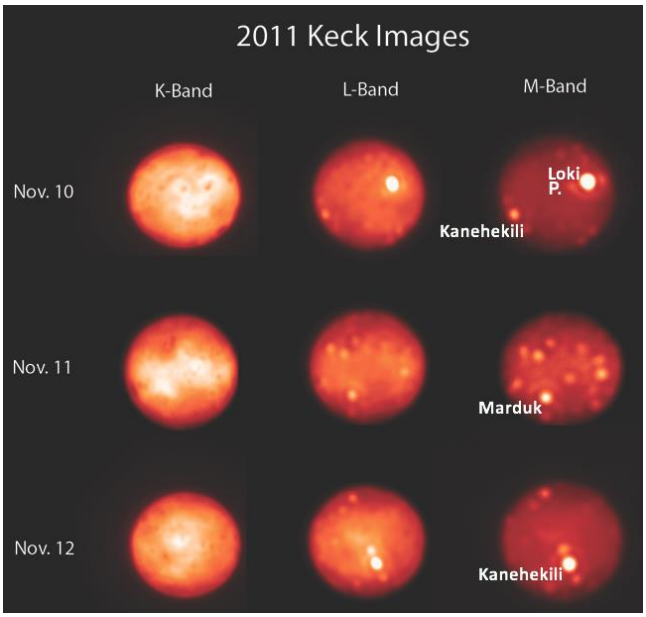

Figure 2:

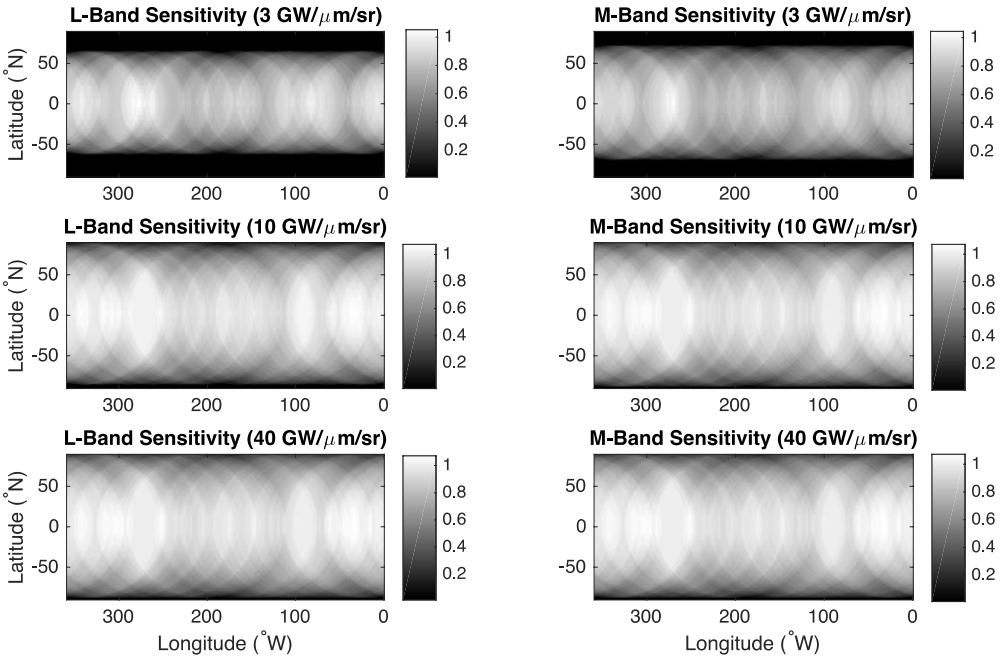

Figure 3:

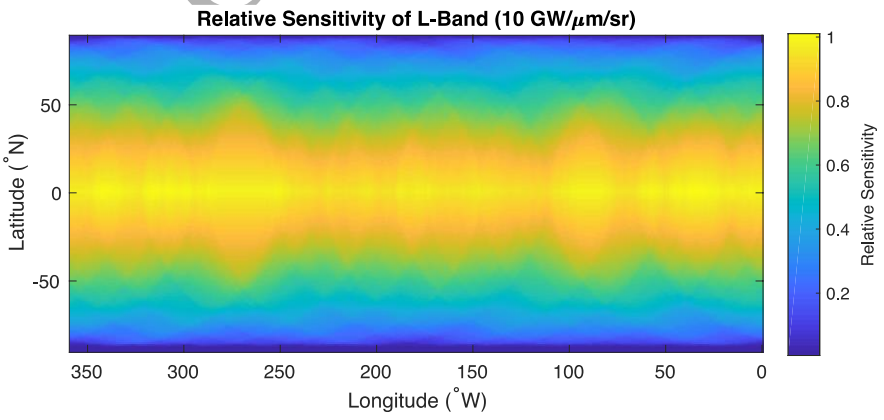

Figure 4:

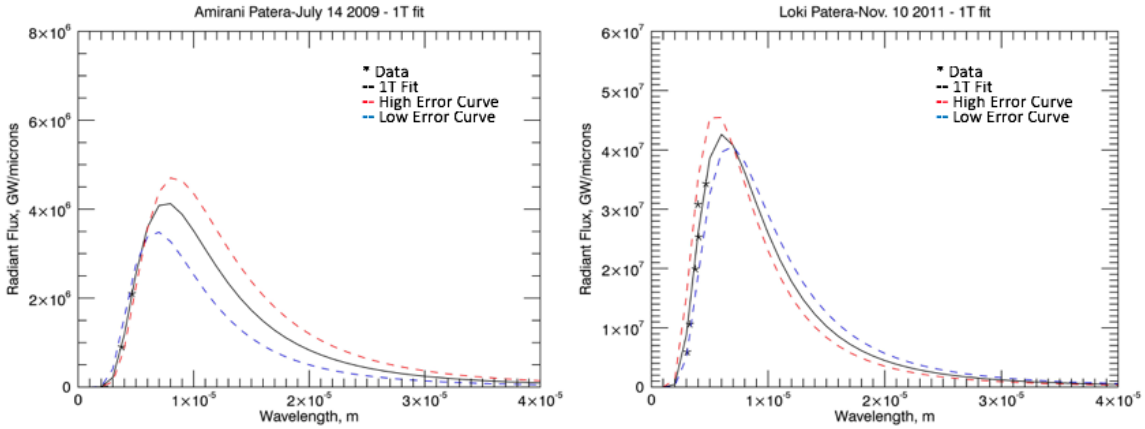

Figure 5:

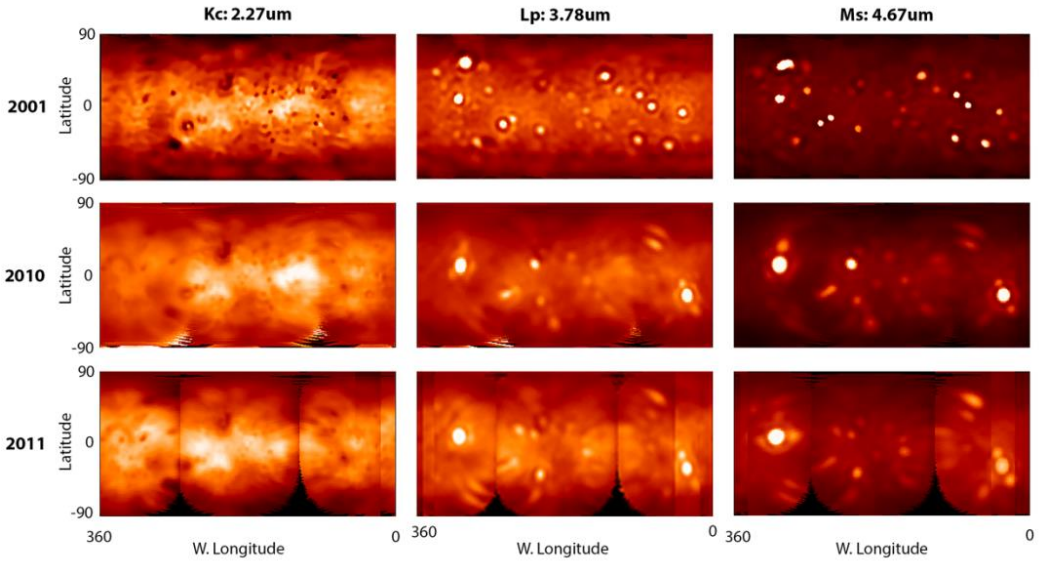

Figure 6:

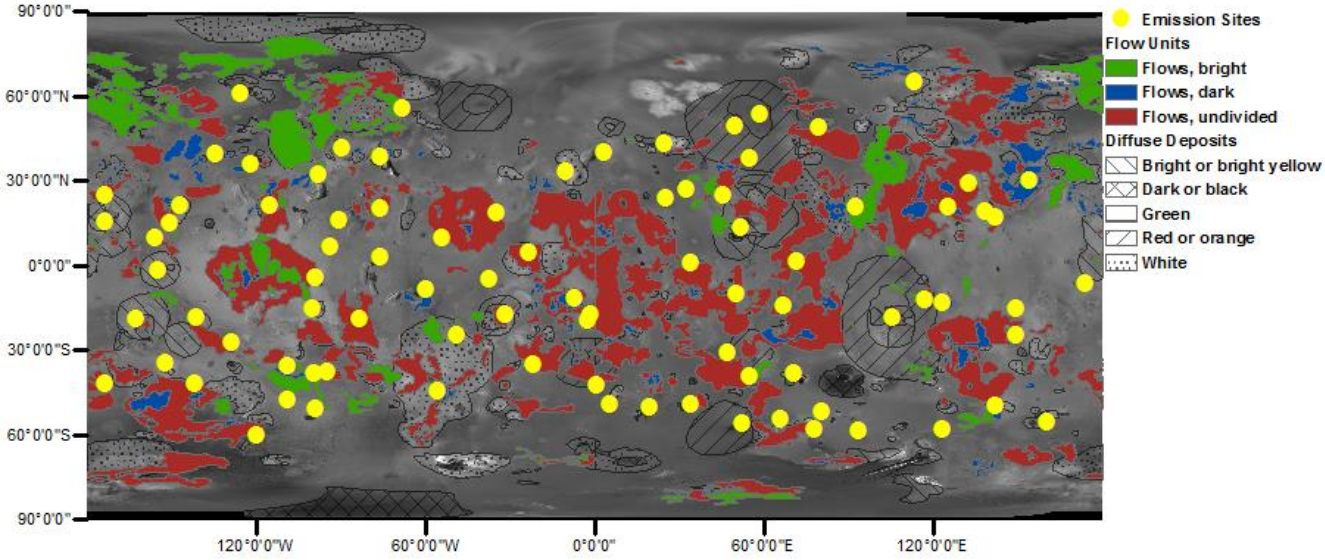

Figure 7:

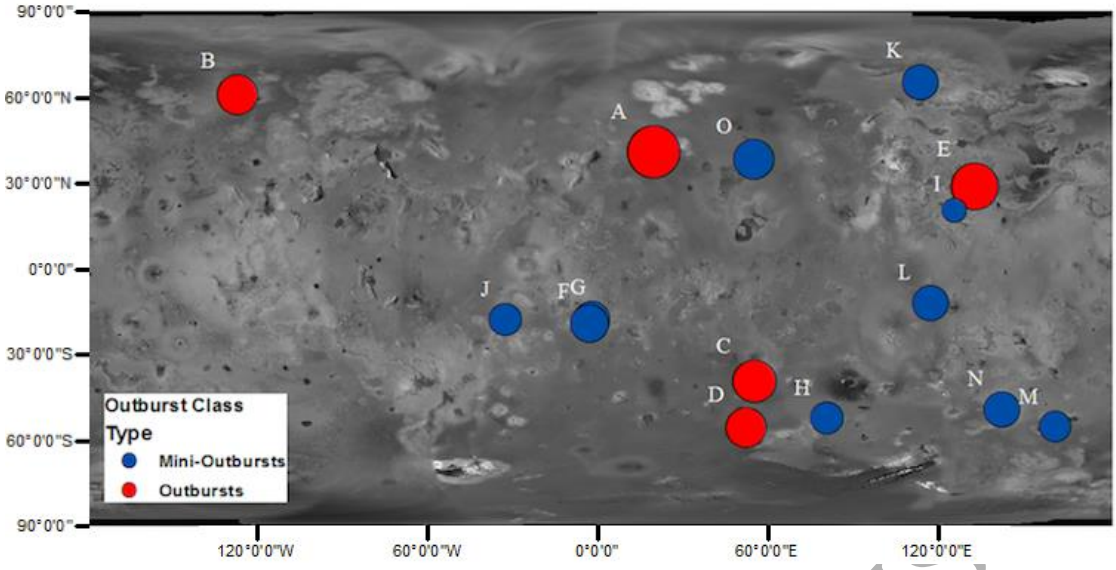

Figure 8:

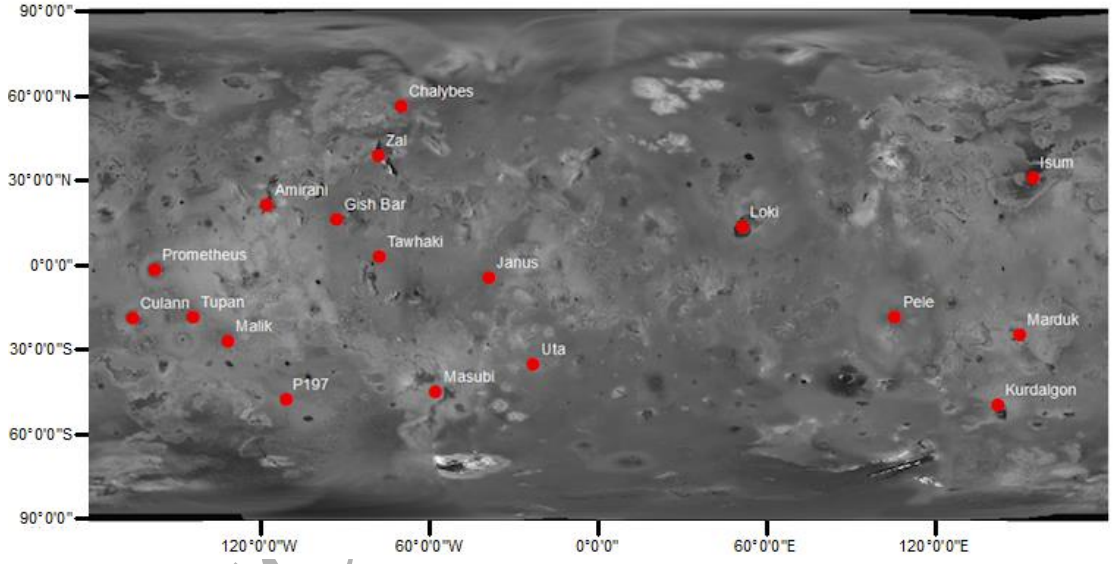

Figure 9:

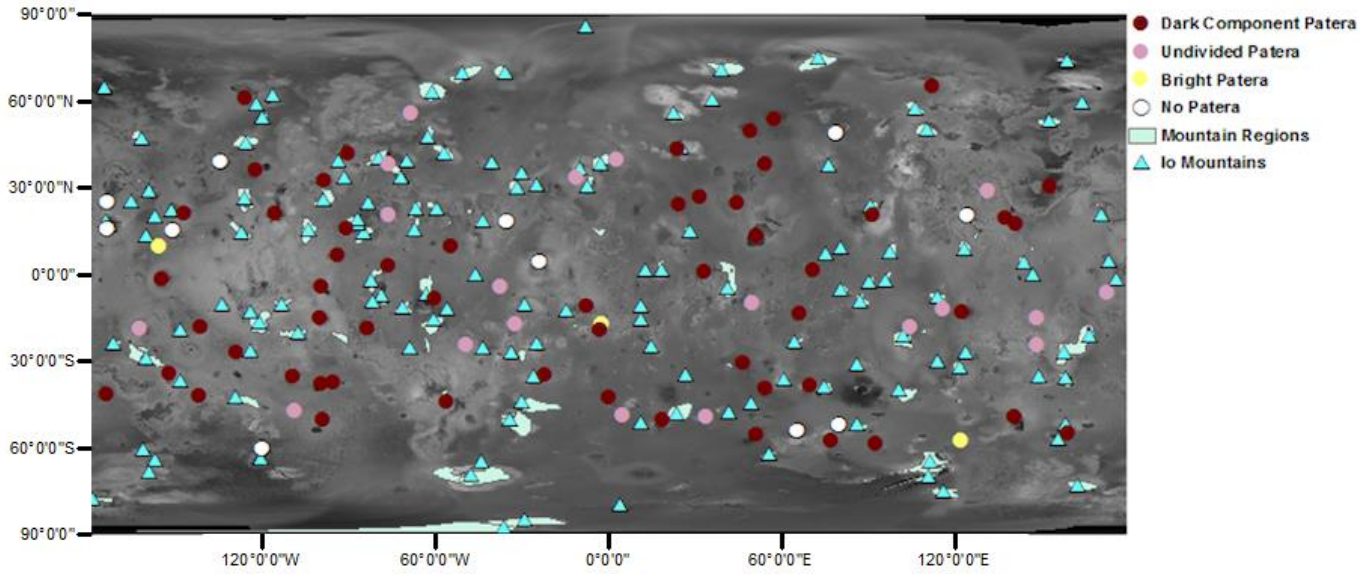

Figure 10:

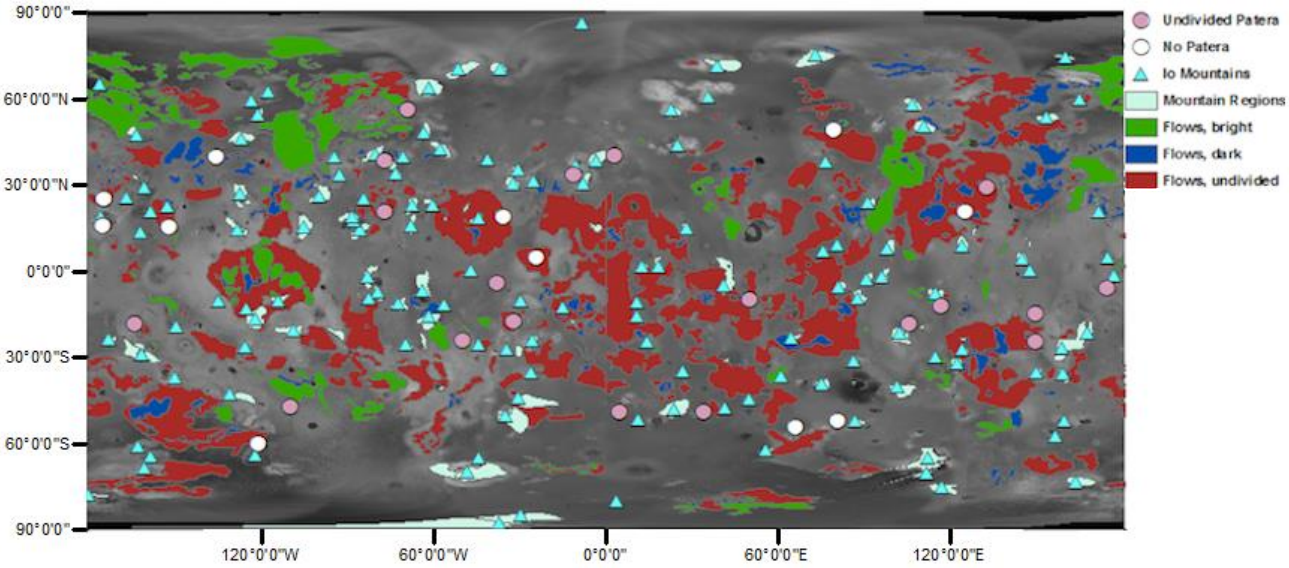

Figure 11:

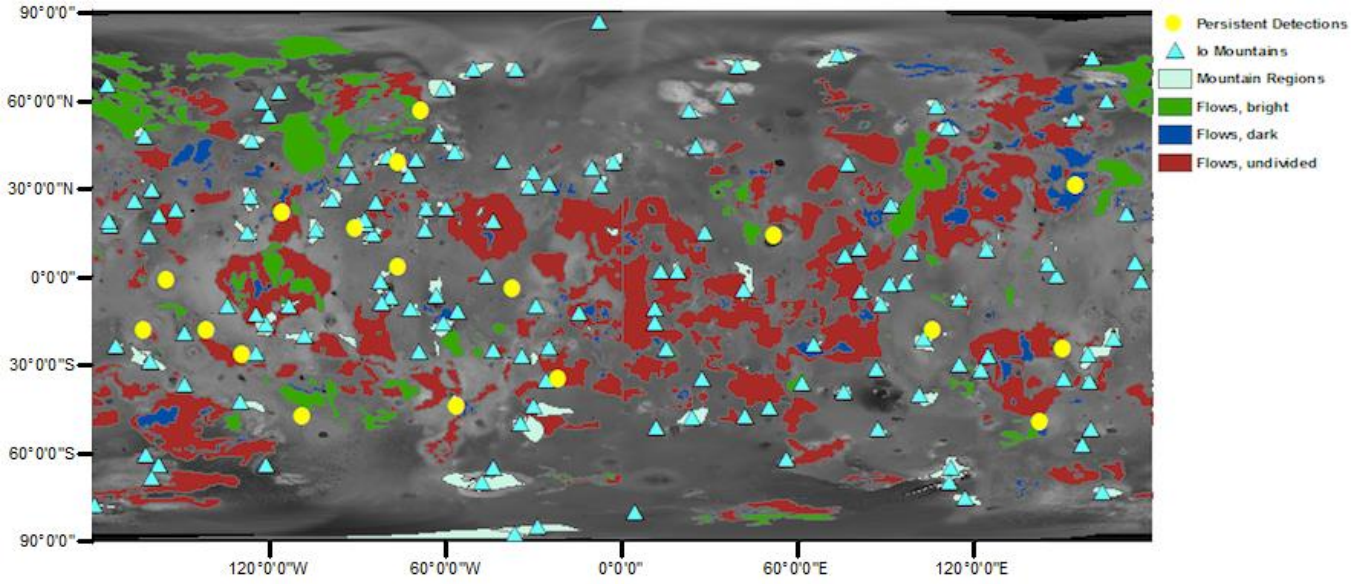

Figure 12:

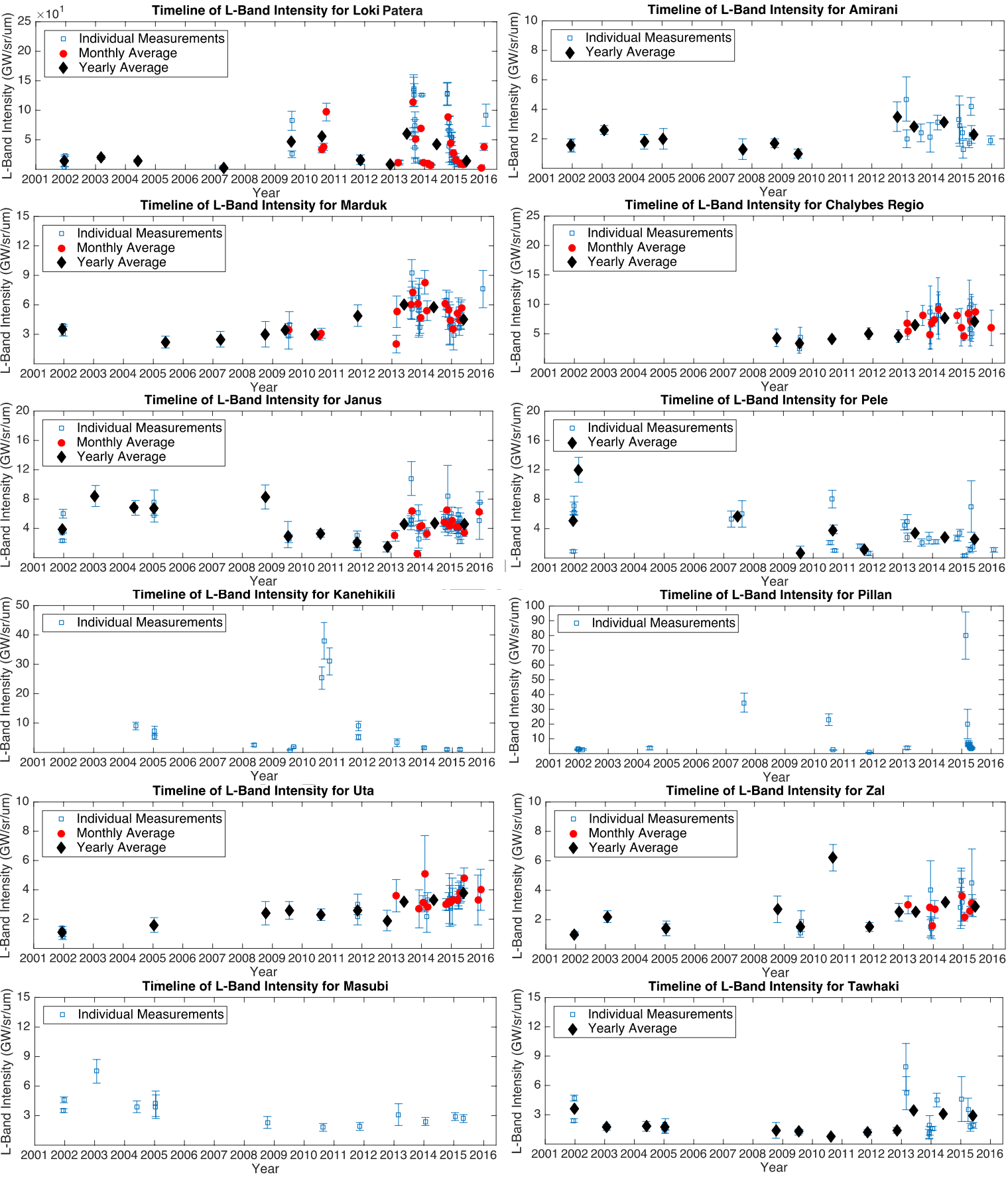
Timeline of L-Band Intensity for Loki Patera
×10^1
Individual Measurements
Monthly Average
Yearly Average
L-Band Intensity (GW/sr/um)
Year
Timeline of L-Band Intensity for Amirani
Timeline of L-Band Intensity for Marduk
Timeline of L-Band Intensity for Chalybes Regio
Timeline of L-Band Intensity for Janus
Timeline of L-Band Intensity for Pele
Timeline of L-Band Intensity for Kanehikili
Timeline of L-Band Intensity for Pillan
Timeline of L-Band Intensity for Uta
Timeline of L-Band Intensity for Zal
Timeline of L-Band Intensity for Masubi
Timeline of L-Band Intensity for Tawhaki

Figure 13:

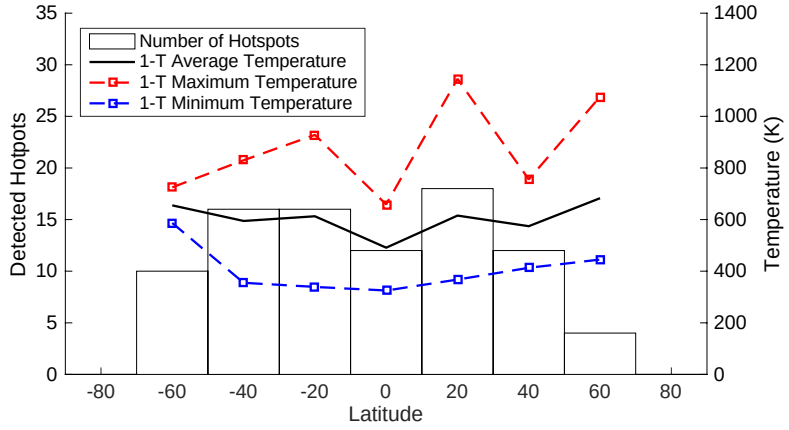

Figure 14:

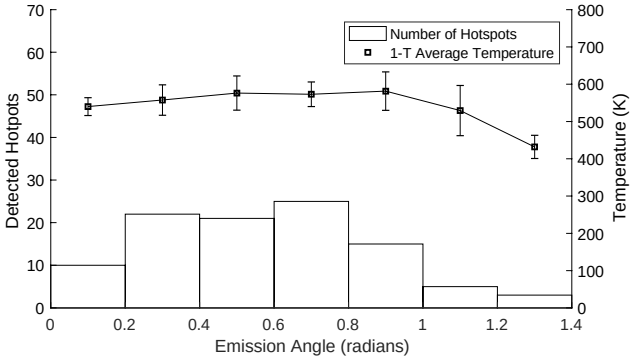

Figure 15:

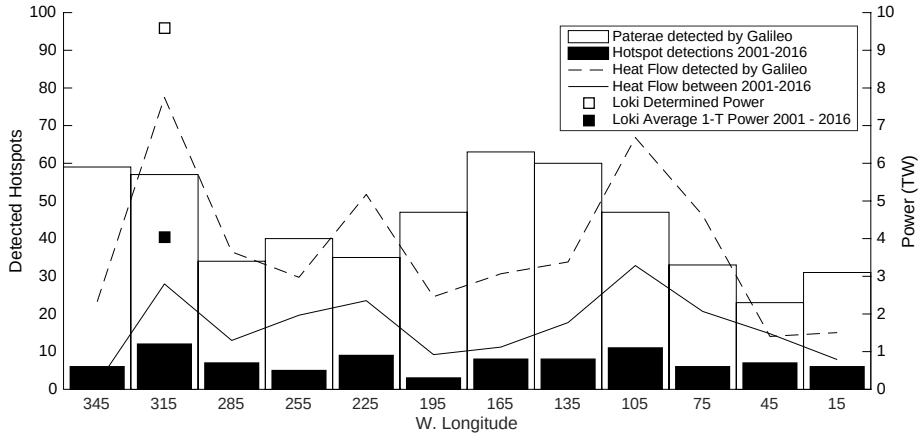

Figure 16:

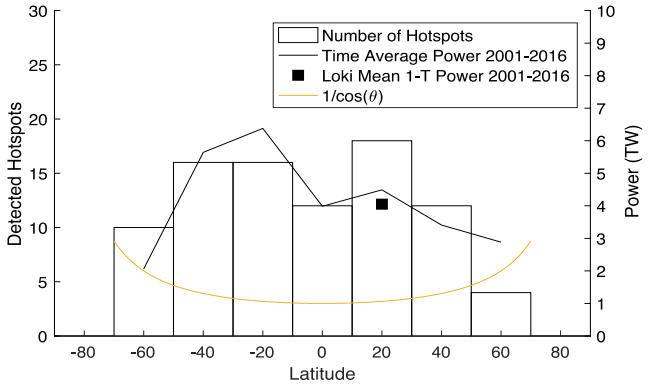

Figure 17:

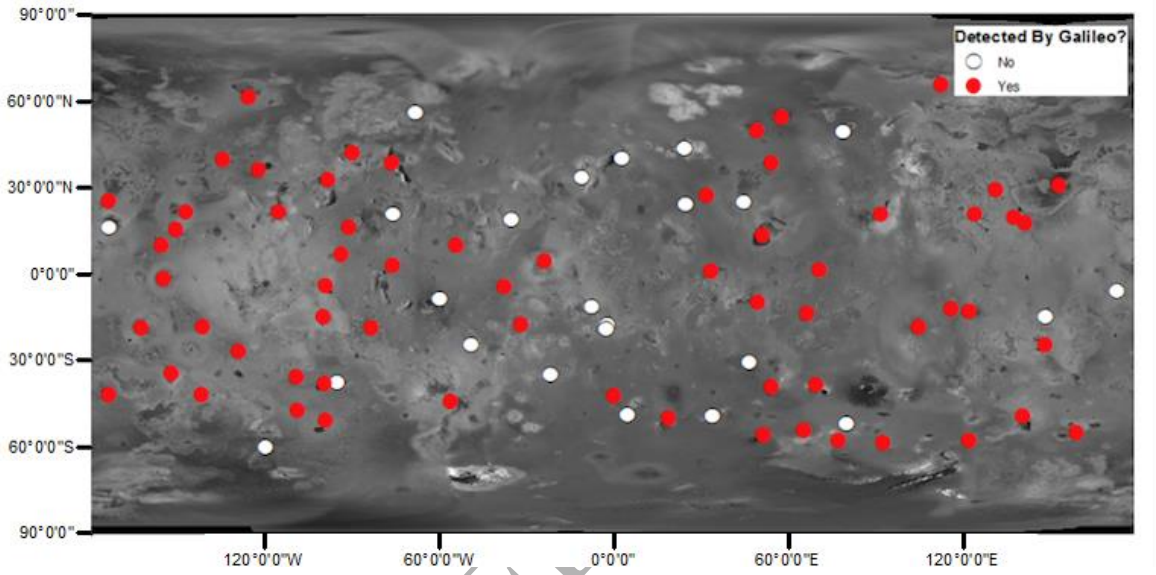

Figure 18:

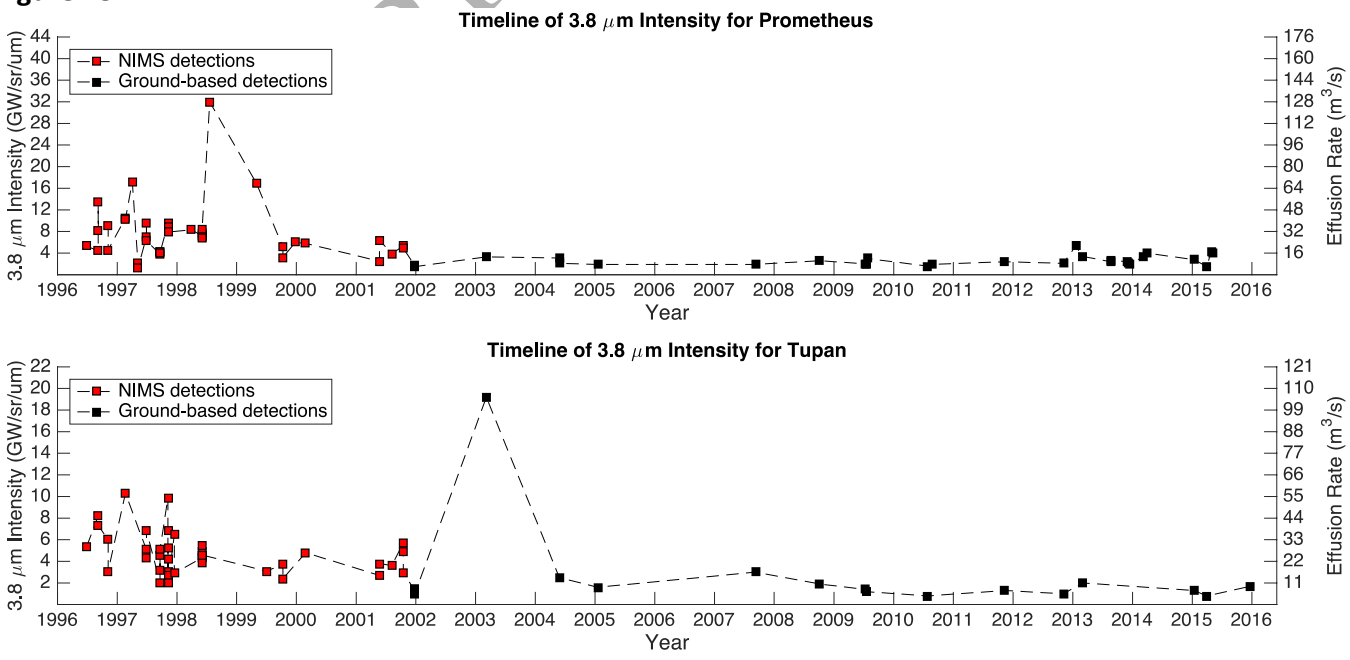

Figure 19:

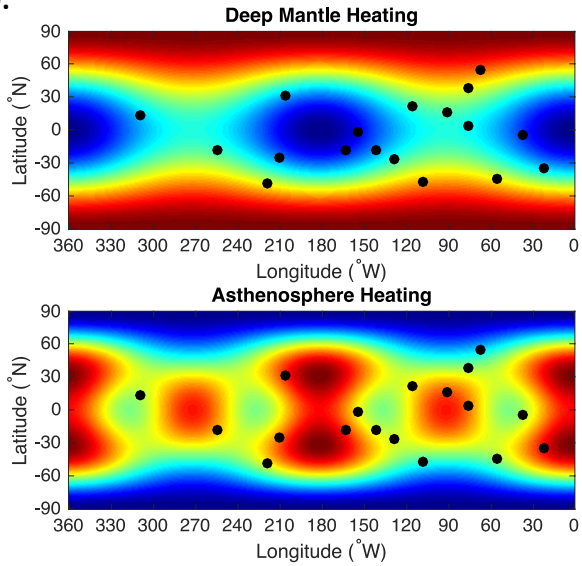

Figure 20:

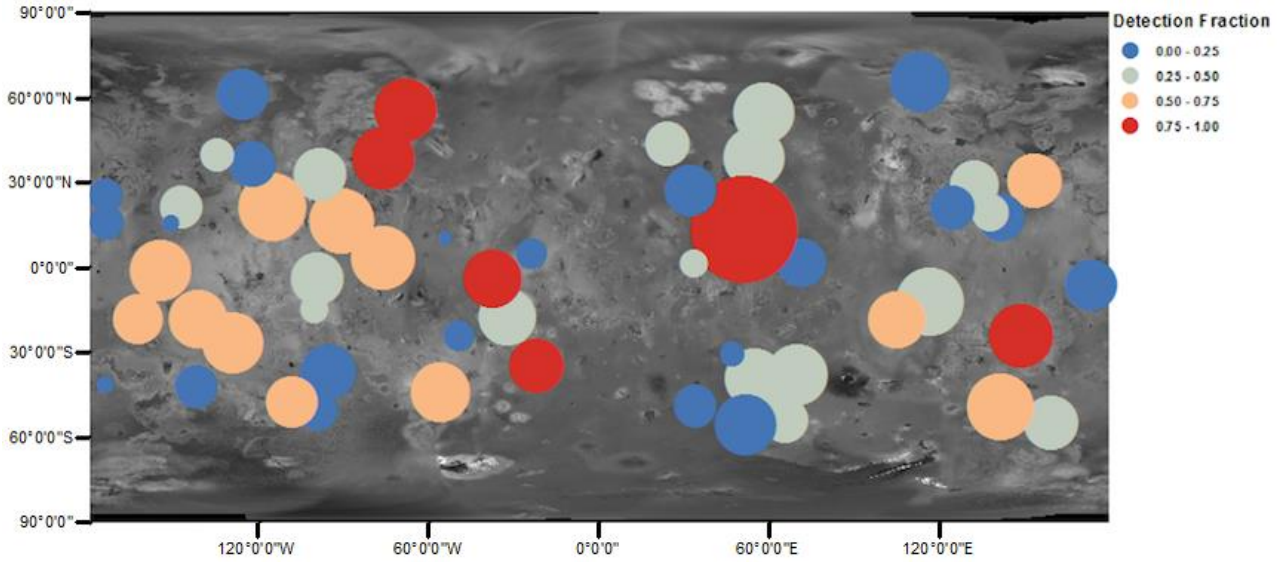

Table 1: Summary of all observations

Year of Observations	Period	Telescope/Instrument	Filters	Publication
2001	Dec. 18-28	Keck II NIRC2	Kc, Lp, Ms	Marchis et al., 2005
2003	Jan. 26 - Mar. 9 (3 nights)	Keck II NIRC2	Kc, Lp, Ms	-[a]
2004	May 27-30 (4 nights)	Keck II NIRC2	Lp, Ms	-[b]
2005	Jan. 15-17 (2 nights)	Keck II NIRC2	Kc, Lp, Ms	-[c]
2007	Feb. 26 - Mar. 1 2007	*New Horizons* LEISA	1.25 - 2.5 μm	Tsang et al., 2014
2007	Apr. 3 - Sep. 9 (3 nights)	Keck II NIRC2	Kc, Lp, Ms	-[d]
2008	Oct. 6-9 (2 nights)	Keck II NIRC2	Kc, Lp, Ms	-[e]
2009	July 14-26 (9 nights)	Keck II NIRC2	Kc, Lp, Ms	-[f]
2010	Sep. 1 - Aug. 30 (13 nights)	Keck ll NIRC2; Gemini N. NIRI	Jc - Ms (6 filters)	de Pater et al., 2014a
2011	Nov. 10-12 (3 nights)	Keck II NIRC2	Hc - Ms (8 filters)	-[g]
2012	Nov. 4-5 (2 nights)	Keck II NIRC2	Kc - Ms (7 filters)	-[h]
2013	Feb. 25 - Mar. 1 (4 nights)	Keck II NIRC2	Y - Ms (10 filters)	-[i]
2013-2015	Aug. 2013 - June 2015 (100 nights)	Keck ll NIRC2; Gemini N. NIRI	Kc - Ms (5 filters)	de Kleer & de Pater, 2016a
2016	Jan. 22	Keck II NIRC2	Kc - Ms (7 filters)	-[j]

[a] Observations of select hot spots in 2003 were published in de Pater et al., 2014a; de Pater et al., 2015a; and de Pater et al., 2017.
[b] Observations of select hot spots in 2004 were published in de Pater et al., 2014a; de Pater et al., 2015a; de Pater et al., 2015b; and de Pater et al., 2017.
[c] Observations of select hot spots in 2005 were published in de Pater et al., 2014a; de Pater et al., 2015a; and de Pater et al., 2017.
[d] Pillan and Pele observations in 2007 were published in de Pater et al., 2015b. Loki observations in 2007 were published in de Pater et al., 2017.
[e] Observations of select hot spots in 2008 were published in de Pater et al., 2014a; de Pater et al., 2015b; and de Pater et al., 2017.
[f] Observations of select hot spots in 2009 were published in de Pater et al., 2014a; de Pater et al., 2015b; and de Pater et al., 2017.
[g] Pillan and Pele observations in 2011 were published in de Pater et al., 2015b. Loki observations in 2011 were published in de Pater et al., 2017.
[h] Loki observations in 2012 were published in de Pater et al., 2017.
[i] Pillan and Pele observations in 2013 were published in de Pater et al., 2015b. Rarog and Heno observations in 2013 were publsihed in de Pater, I. et al., 2014b. Loki observations in 2013 were published in de Pater et al., 2017.
[j] Loki observations in 2016 were published in de Pater et al., 2017.

Table 2: Wavelength ranges of filters used

Filter	Wavelength (μm)	Wavelength range (μm)
Keck		
Kc	2.27	2.256 - 2.285
H_2O	3.06	2.986 - 3.140
PAH	3.29	3.263 - 3.318
Lp	3.78	3.426 - 4.126
BRα-cont.	3.99	3.952 - 4.021
BRα	4.05	4.018 - 4.086
Ms	4.68	4.549 - 4.790
Gemini		
Jc	1.07	1.062 - 1.076
CH4L	1.69	1.610 - 1.780
BRγ	2.16	2.14 - 2.195
Lp	3.78	3.430 - 4.130
Mp	4.68	4.550 - 4.790

Table 3: All outbursts and mini-outbursts detected since 2001, ordered by date of detection

Outbursts

UT date	Position	Name	Temperature (K)	Area (km^2)	Wavelength (μm)	Power (TW)	Publication	Label
2001/02/20	340.0W, 41.0N	Surt	1240	445	1.2 - 2.2	78	Marchis et al., 2002	A
2007/03/01	121.0W, 61.0N	Tvashtar Patera	1200	37	1.25 - 2.5	4.9	Laver et al., 2007	B
2013/08/15	306.0W, 38.7S	Rarog Patera	1100	71	1.2 - 4.7	10	de Pater et al., 2014b	C
2013/08/15	307.2W, 56.0S	Heno Patera	720	220	1.2 - 4.7	4.7	de Pater et al., 2014b	D
2013/08/29	223.5W, 29.1N	201308C	1900	58	2.2 - 4.7	24.5	de Kleer, K. et al., 2014	E

Mini-Outbursts

UT date	Position	Name	Temperature (K)	Area (km^2)	Wavelength (μm)	Power (GW)	Publication	Label
2004/05/30	2.6W, 19.2S	Sui Jen Patera	1075	7	2.2 - 4.7	3500	de Pater et al., 2015	F
2004/05/30	0.9W, 18.3S	Tung Yo Patera	>1100	6	2.2 - 4.7	2000	de Pater et al., 2015	G
2004/05/31	272.0W, 40.8S	S. of Babbar	>900	28	2.2 - 4.7	1200	de Pater et al., 2015	H
2007/02/27	236.0W, 21.0N	East Girru	1100	2	1.2 - 2.5	200	Tsang et al., 2014	I
2007/08/14	245.2W, 8.5S	Pillan Patera	840	>17	2.2 - 4.7	500	de Pater et al., 2016	–
2010/06/28	245.2W, 8.5S	Pillan Patera	600-700	60	2.2 - 4.7	600	de Pater et al., 2016	–
2010/08/21	32.0W, 18.5S	Kanehekili Fluctus	520	235	2.2 - 4.7	1000	de Pater et al., 2014a	–
2010/11/23	32.0W, 18.5S	Kanehekili Fluctus	525	280	1.1 - 4.7	1200	de Pater et al., 2014a	J
2014/10/31	246.9W, 64.8N	Chors Patera	397.5	2189.8	1.2 - 4.7	3100.3	de Kleer and de Pater, 2016a	K
2015/01/10	266.2W, 58.1S	Mithra Patera	–[a]	–	3.8	–	de Kleer and de Pater, 2016a	–
2015/01/26	219.4W, 48.6S	Kurdalagon Patera	1183.5	8.6	2.3, 3.8, 4.7	952.8	de Kleer and de Pater, 2016a	–
2015/03/31	245.4W, 11.5S	Pillan Patera	391.7	695.1	1.2 - 4.7	928.3	de Kleer and de Pater, 2016a	L
2015/04/01	198.1W, 50.0S	Sethlaus/Gabija Paterae	616.3	85.8	1.2 - 4.7	702.1	de Kleer and de Pater, 2016a	M
2015/04/05	221.2W, 48.8S	Kurdalagon Patera	1287.4	8.0	1.2 - 4.7	1250.8	de Kleer and de Pater, 2016a	N
2015/12/25	304.3W, 38.2N	Amaterasu Patera	412.2	3265.4	1.2 - 4.7	5346.4	de Kleer and de Pater, 2016a	O

[a] Observed only at L-Band.

Table 4: All hot spots detected using adaptive optics between 2001 and 2016

Hotspot	Average Latitude	Average W. Longitude	Patarae Association	Detection Fraction	Max 3.8μm Intensity	Average 3.8μm Intensity	Detections During Voyager/Galileo Era[a]
201308C	29.0	227.9	Undivided	0.26	>500	71.2	NIMS
Aluna Patera	41.7	89.9	Undivided, Dark	0.13	4.6	3.2	SSI, NIMS
Amaterasu Patera	38.2	305.3	Dark, Undivided	0.27	43.1	21.7	NIMS, PPR
Amirani	21.2	115.5	Dark	0.68	4.7	2.3	NIMS, SSI, Keck
Catha Patera	-50.5	99.1	Dark	0.13	-	-	NIMS
Chaac Patera	9.8	155.9	Undivided, Bright	0.06	0.9	-	NIMS
Chalybes Regio	55.1	68.1	Undivided	0.82	9.9	6.7	-
Chors Patera	65.3	247.0	Dark	0.18	57.0	24.7	PPR
Creidne Patera	-50.1	341.0	Dark, Undivided	0.05	15.0	-	PPR
Culann Patera	-18.6	162.8	Undivided	0.64	3.7	1.6	NIMS, SSI
Daedulus Patera	20.8	267.8	Dark	0.1	-	-	PPR?
Dazhbog Patera	54.0	301.9	Dark	0.16	12.7	8.6	PPR
Dusura Patera	36.2	122.4	Dark	0.14	8.1	7.5	NIMS
East Girru	20.7	235.2	None	0.28	5.4	4.7	NIMS, SSI, PPR
Estan Patera	20.5	76.2	Undivided	0.12	-	-	-
Euboea	-48.8	355.0	Undivided	0.07	8.6	-	Voyager
Fuchi Patera	27.0	327.8	Dark	0.15	1.1	1.0	SSI, PPR
Gabija/Sethlaus Paterae	-55.0	200.0	Dark	0.27	32.6	11.7	NIMS
Gibil Patera	-13.8	293.2	Dark, Undivided	0.05	3.4	-	PPR
Gish Bar Patera	16.1	90.9	Dark, Undivided	0.59	5.4	3.3	NIMS, SSI
Heno Patera	-55.6	308.2	Dark, Undivided	0.2	270.0	70.5	PPR
Hephaestus Patera	1.5	288.7	Dark, Undivided	0.13	1.0	0.8	PPR
Isum Patera	30.5	206.2	Dark	0.52	6.2	3.3	NIMS, SSI, PPR
Itzamma Patera	-14.9	100.1	Dark, Undivided	0.3	2.7	1.4	NIMS
Janus Patera	-4.4	37.5	Undivided	1.0	10.8	4.6	NIMS, SSI
Kanehekili Fluctus	-17.4	31.9	Undivided (Multiple)	0.32	25.3	9.5	NIMS, SSI
Kinich Ahau Patera	49.6	310.4	Dark	0.06	-	-	PPR
Kurdalagon Patera	-49.3	218.5	Dark	0.59	68.0	21.3	NIMS, PPR
Loki Patera	13.4	308.5	Dark, Undivided, Bright	1.0	136.0	38.2	NIMS, SSI, PPR
Malik Patera	-26.9	129.2	Dark,Undivided	0.62	6.6	2.4	NIMS
Marduk Fluctus	-24.6	210.8	Undivided	1.0	8.3	4.8	NIMS, SSI, PPR
Masubi Fluctus	-44.3	56.2	Dark	0.66	7.5	3.4	NIMS, SSI
Mazda Patera	-10.0	310.0	Undivided (Multiple)	0.06	-	-	PPR
Mithra Patera	-58.4	267.0	Dark	0.25	55.0	25.6	SSI, PPR
Mulungu Patera	17.4	218.0	Dark	0.18	11.6	6.2	NIMS, SSI, PPR
N. Lerna Regio	-54.1	294.2	None	0.4	7.1	4.5	PPR
NIMSI32D	-41.7	174.0	Dark, Undivided	0.21	1.6	1.4	NIMS
NIMSI32J	-18.8	83.5	Dark, Undivided	0.06	2.1	-	NIMS
P123	-41.9	141.9	Dark	0.15	2.5	-	NIMS
P197	-47.3	108.9	Undivided	0.52	11.7	6.2	NIMS
P207	-37.4	95.3	Dark	0.16	5.0	-	Keck
P98	-15.0	211.1	Undivided	0.07	-	-	-
Paive Patera	-42.3	359.6	Dark, Undivided	0.09	1.0	-	Voyager
Pele	-18.4	254.7	Undivided	0.62	6.1	3.6	NIMS, SSI, PPR
PFd224	-38.1	99.6	Dark	0.14	0.4	-	NIMS
PFd267	-35.5	109.3	Dark	0.07	-	-	NIMS
PFd535	-8.5	59.9	Dark, Undivided	0.14	-	-	-
PFd681	6.6	93.9	Dark, Bright	0.06	2.2	2.1	NIMS
PFd717	10.0	54.2	Dark	0.13	1.5	1.4	SSI?
PFd1746	-11.2	7.3	Dark	0.06	7.5	-	Voyager
PFu374	-24.3	49.2	Undivided	0.25	3.1	-	-
PFu1063	40.0	357.0	Undivided	0.14	2.4	-	-
Pfu1410	-6.1	186.4	Undivided (Multiple)	0.15	1.4	1.2	-
Pillan Patera	-12.0	243.5	Undivided	0.45	34.5	7.1	NIMS, SSI, PPR
Prometheus	-1.6	155.0	Dark	0.73	5.3	2.6	NIMS, SSI
PV47	49.0	280.6	None	0.06	-	-	-
PV98	25.0	315.0	Dark	0.06	1.3	1.0	NIMS
PV129	24.0	335.0	Dark	0.07	-	-	NIMS
PV170	-49.1	326.0	Bright or Undivided	0.17	11.7	7.1	-
Pyerun Patera	-57.7	237.1	Bright	0.1	-	-	Voyager IRIS
Rarog Patera	-39.2	305.4	Dark, Undivided	0.32	320.0	29.0	PPR
Reiden Patera	-13.0	237.0	Dark	0.06	-	-	NIMS, SSI, PPR
S. of Babbar	-51.8	279.6	None	0.11	4.0	2.9	-
Sengen Patera	-30.6	313.1	Dark	0.09	1.3	-	-
Shamash Patera	-34.5	152.5	Dark, Undivided	0.15	1.5	-	NIMS
Shango Patera	32.5	98.4	Dark	0.28	6.1	4.8	NIMS
Sigurd Patera	-4.1	99.2	Dark	0.33	6.0	4.1	NIMS
Sobo	15.3	151.0	None	0.19	1.6	1.2	NIMS
Sui Jen Patera	-19.2	2.5	Dark	0.09	-	-	-
Surt	43.4	335.6	Dark	0.37	3.8	2.0	HST, Keck
Surya Patera	21.3	147.2	Dark	0.26	3.6	2.4	NIMS
Susanoo/Mulungu Paterae	19.4	221.9	Dark	0.31	3.8	1.9	NIMS, SSI, PPR
Tawhaki Patera	3.0	76.1	Dark	0.69	7.9	2.4	NIMS, SSI
Thor	39.5	134.6	None	0.42	1.6	1.2	NIMS
Tol Ava Patera	0.9	326.3	Undivided, Dark	0.26	8.4	4.5	PPR
Tung Yo Patera	-17.4	1.9	Two Sites: Bright and None	0.06	72.0	39.1	-
Tupan Patera	-18.4	141.5	Bright, Dark, Undivided	0.7	19.2	2.6	NIMS
Tvashtar Paterae	60.9	125.7	Bright, Dark, Undivided	0.07	40.8	-	NIMS
Ukko Patera	33.5	18.8	Undivided	0.14	1.4	-	Voyager
Ulgen Patera	-38.2	289.8	Dark	0.43	3.2	2.6	NIMS, PPR
Unidentified23W	4.5	23.7	None	0.14	1.7	1.4	SSI
Unidentified35W	18.8	35.2	None	0.08	-	-	-
Unidentified4646	-60.0	120.0	None	0.05	-	-	-
Uta Patera	-34.8	21.9	Dark	0.81	4.8	3.0	Keck
Viracocha Patera	-57.8	282.4	Bright, Dark	0.07	-	-	Voyager
Volund	25.1	173.8	None	0.14	1.5	-	SSI, NIMS
Zal Patera	38.4	76.3	Undivided	0.82	6.2	2.6	NIMS, SSI
Zamama	15.8	173.9	None	0.25	1.4	1.3	NIMS

[a] Detections provided in Io Geodatabase (Williams et al., 2011a)

Table 5: Total L-band intensity and total power output from detected hot spots at each observation period

Year of Observations	Longitudinal Coverage	Hotspot Detections	Total L-Band Intensity (GW/sr/μm)	Total L-Band Intensity w/o Loki (GW/sr/μm)	Total (GW) Power	Total Power w/o Loki (GW)
2001	Full	26	90	71	-	-
2003	0W - 215W, 260W - 360W	19	80	60	-	-
2004	Full	22	160	145, 72* (excluding Tung Yo)	-	-
2005	0W - 180W, 320W - 360W	16	-	45	-	1196
2007 (New Horizons)	Full	37	-	-	-	-
2007	70W - 330W	19	115	111, 50* (excluding Pillan, Tvashtar)	8533	3587, 2077*
2008	0W - 230W, 320W - 360W	22	-	53	-	2407
2009	Full	27	70	45	3970	2074
2010	Full	22	110	73	-	-
2011	Full	23	73	53	3402	2163
2012	0W - 200W, 260W - 360W	27	53	45	-	-
2013	Full	22	80	68	3734	2265
2013-2015	Full	48	-	-	-	-
2016	200W - 340W	7	-	-	-	-

Table A1: Detections made by Keck between 2003 and 2016 excluding those published in de Kleer and de Pater (2016a;b)

Date	Attributed Hotspot	W. Longitude	Latitude	Kc (2.27μm) Intensity (GW/sr/μm)	PAH (3.29μm) Intensity (GW/sr/μm)	Lp (3.78μm) Intensity (GW/sr/μm)	BRA (4.05μm) Intensity (GW/sr/μm)	Ms (4.68μm) Intensity (GW/sr/μm)	1-T Fit Temp. (K)	1-T Power (GW)
2004/05/28	Amaterasu	307.0±1.7	38.5±1.8			5.5±1.0		28.0±4.0		
2010/07/27	Amaterasu	302.0±2.5	38.0±1.7			3.5±0.5		7.0±1.0	415^{+55}_{-40}	365^{+280}_{-120}
2016/01/22	Amaterasu	305.0±3.1	38.7±3.0			16.6±4.4		28.9±9.3	431^{+89}_{-51}	1328^{+1594}_{-571}
2003/01/26	Amirani	111.4±0.8	21.7±1.5			2.6±0.3		3.6±0.8	526^{+83}_{-46}	101^{+47}_{-28}
2003/01/26	Amirani	115.7±2.2	22.9±2.0					3.1±0.6		
2004/05/27	Amirani	117.7±2.5	21.4±2.8			1.8±0.5		3.4±0.7		
2005/01/15	Amirani	114.0±1.0	22.6±1.6					6.8±2.1		
2005/01/17	Amirani	113.9±1.8	22.8±1.5			2.0±0.7		5.9±1.1	340^{+25}_{-17}	716^{+403}_{-248}
2007/09/09	Amirani	117.5±2.7	20.1±2.5			1.3±0.7		4.8±1.0		
2008/10/06	Amirani	117.7±2.1	20.2±2.4			1.7±0.3		3.3±0.6	433^{+44}_{-25}	150^{+62}_{-45}
2009/07/14	Amirani	114.6±1.1	20.9±1.3			0.8±0.2		2.1±0.4	382^{+33}_{-22}	150^{+79}_{-49}
2009/07/14	Amirani	113.3±1.7	22.2±1.4			1.3±0.4		2.5±0.4	426^{+32}_{-34}	122^{+77}_{-33}
2012/11/04	Amirani	116.4±2.1	21.8±1.9		1.0±0.4	3.5±1.0	5.4±1.0	8.9±1.5	409^{+43}_{-42}	497^{+509}_{-159}
2013/02/25	Amirani	115.1±1.9	20.2±2.2			4.7±1.5	2.3±0.6	3.1±1.4	1296^{+581}_{-560}	80^{+332}_{-41}
2013/03/01	Amirani	118.1±1.5	21.5±1.7			2.0±0.6	2.8±0.7	3.4±0.7	476^{+144}_{-86}	120^{+50}_{-28}
2012/11/04	Catha	103.4±2.3	-50.9±2.4				3.8±1.5	6.1±1.2	420^{+176}_{-77}	307^{+842}_{-147}
2013/02/25	Catha	94.8±5.2	-50.0±5.1				2.5±0.6	2.7±0.5	752^{+94}_{-74}	54^{+11}_{-15}
2011/11/11	Chaac	155.9±3.4	9.8±3.4			0.9±0.1	2.2±0.5	2.3±0.5	507^{+53}_{-34}	72^{+26}_{-13}
2008/10/09	Chalybes Regio	70.4±2.8	54.1±2.6			4.3±1.5		3.0±1.1	1082^{+165}_{-264}	72^{+10}_{-12}
2009/07/14	Chalybes Regio	77.4±3.5	52.1±3.7			2.4±0.7		2.4±0.4	665^{+125}_{-67}	52^{+14}_{-8}
2009/07/26	Chalybes Regio	66.0±1.0	54.0±1.4			4.4±1.7		5.1±0.9	609^{+80}_{-52}	117^{+34}_{-21}
2010/08/21	Chalybes Regio	68.9±4.5	56.0±2.5			4.1±0.6		5.4±0.8	545^{+110}_{-70}	145^{+80}_{-35}
2011/11/12	Chalybes Regio	65.4±3.8	53.3±4.1			4.5±0.9		9.0±1.7	500^{+55}_{-38}	267^{+127}_{-41}
2011/11/12	Chalybes Regio	67.6±5.3	53.5±5.2			5.5±1.2		9.2±1.6	479^{+99}_{-53}	316^{+151}_{-74}
2012/11/04	Chalybes Regio	80.7±2.8	52.3±3.0			4.6±1.1	5.5±1.2	7.4±1.3	481^{+107}_{-32}	253^{+103}_{-85}
2013/02/25	Chalybes Regio	68.8±1.9	55.0±2.0			6.7±2.1	6.0±0.6	7.6±1.4	590^{+234}_{-174}	174^{+591}_{-55}
2013/03/01	Chalybes Regio	88.0±2.8	53.9±2.7			5.5±1.5	3.5±0.8	5.1±1.9	557^{+162}_{-125}	122^{+40}_{-26}
2004/05/28	Creidne	341.1±1.9	-50.1±2.0			15.0±3.0		53.0±8.0		
2004/05/29	Culann	164.7±2.4	-16.4±3.0			1.4±0.5		2.3±0.5		
2008/10/06	Culann	163.7±1.6	-18.4±1.8			1.3±0.7		1.4±0.2	646^{+150}_{-59}	31^{+7}_{-5}
2009/07/16	Culann	160.1±2.3	-19.5±2.0			1.0±0.3		1.8±0.4	450^{+77}_{-38}	75^{+52}_{-27}
2010/08/22	Culann	160.5±2.5	-17.4±1.7					1.0±0.2		
2011/11/11	Culann	161.2±2.4	-19.6±2.7			0.9±0.3	1.0±0.2	1.3±0.2	502^{+161}_{-54}	39^{+31}_{-9}
2012/11/04	Culann	159.0±2.6	-16.6±3.2			1.2±0.3	1.3±0.8	1.6±0.3	605^{+199}_{-91}	38^{+22}_{-7}
2013/03/01	Culann	167.6±2.5	-21.2±2.4			3.6±1.1	3.3±0.7	3.5±0.8	707^{+304}_{-204}	69^{+106}_{-2}
2009/07/25	Daedulus	261.6±1.9	21.2±1.9					1.7±0.8		
2003/03/09	Dazhbog	305.5±2.2	54.2±2.1			3.3±0.6				
2007/04/03	Dazhbog	292.1±1.7	51.5±2.1					4.5±0.8		
2007/04/08	Dazhbog	298.1±2.2	54.6±1.9					7.9±1.8		
2011/11/11	East Girru	124.0±2.2	19.9±2.6		3.0±0.7	3.9±1.0	4.0±0.7	2.8±0.5	785^{+11}_{-62}	67^{+7}_{-1}
2009/07/14	Estan	77.3±2.2	19.0±2.4					1.0±0.2		
2004/05/30	Euboea	355.0±2.7	-50.0±3.0			8.6±1.5		17.6±3.5		
2012/11/05	Fuchi	327.0±3.0	27.9±3.7			0.9±0.2	0.9±0.3	1.7±0.3	449^{+111}_{-56}	69^{+72}_{-27}
2012/11/05	Gibil	293.2±2.4	-13.8±2.1		3.2±0.7	3.3±0.5	3.7±0.7	4.4±0.7	646^{+62}_{-51}	93^{+19}_{-12}
2003/01/26	Gish Bar	88.6±1.8	16.5±1.8			1.8±0.6		2.9±0.7	474^{+73}_{-41}	102^{+60}_{-34}
2005/01/17	Gish Bar	88.5±2.9	17.6±2.7					1.4±0.6		
2008/10/09	Gish Bar	92.8±0.6	14.9±1.1			5.3±1.4		6.0±1.2	619^{+127}_{-59}	135^{+45}_{-28}
2012/11/04	Gish Bar	92.4±2.7	15.5±2.9				1.0±0.5	0.8±0.2	656^{+293}_{-156}	18^{+24}_{-2}
2004/05/27	Gish Bar	93.5±1.0	18.4±1.7			1.2±0.2		2.6±0.5		
2004/05/29	Isum	207.6±2.9	30.4±3.1			3.5±1.6		3.3±0.6		
2007/04/03	Isum	201.1±1.1	33.0±1.1			6.1±1.2		5.0±0.9	863^{+272}_{-104}	101^{+2}_{-2}
2008/10/06	Isum	198.7±2.5	25.2±3.0					2.1±0.5		
2009/07/25	Isum	207.0±1.6	31.4±1.6			2.1±0.7		1.7±0.4	873^{+289}_{-128}	35^{+6}_{-2}
2010/08/22	Isum	207.7±2.5	31.6±1.7			1.8±0.3		2.4±0.4	540^{+125}_{-75}	65^{+40}_{-20}
2011/11/11	Isum	207.8±2.1	29.0±2.2			2.8±0.5	3.3±0.6	2.5±0.4	634^{+12}_{-43}	66^{+9}_{-2}
2013/02/26	Isum	203.1±1.9	33.7±2.1				7.9±1.2	1.6±0.3		
2013/03/01	Isum	198.9±3.5	30.0±3.4				2.1±0.7	2.3±0.6		
2007/09/09	Itzamma	103.3±2.0	-14.3±2.1			1.3±0.4		1.0±0.3	920^{+106}_{-190}	21^{+15}_{-7}
2009/07/14	Itzamma	98.6±1.2	-15.5±1.5			0.7±0.1		0.8±0.1	620^{+123}_{-64}	20^{+7}_{-4}
2012/11/04	Itzamma	99.1±2.8	-15.0±2.5			1.1±0.3	1.4±0.3	1.5±0.2	626^{+222}_{-96}	35^{+19}_{-5}
2003/01/26	Janus	37.7±1.4	-4.4±1.5	6.7±4.0		8.4±1.4		7.6±1.4	887^{+223}_{-173}	146^{+64}_{-9}
2004/05/30	Janus	37.7±2.2	-3.5±2.2			6.8±1.0		7.8±1.0		
2005/01/15	Janus	36.6±1.2	-3.4±1.6			7.5±1.7		12.1±3.0	474^{+76}_{-41}	429^{+261}_{-149}
2005/01/17	Janus	42.3±1.7	-5.0±2.4			5.8±0.9		6.7±1.8	606^{+171}_{-74}	153^{+80}_{-39}
2008/10/09	Janus	40.8±1.6	-4.4±1.3	2.4±0.6		8.2±1.6		7.1±1.4	728^{+50}_{-70}	151^{+30}_{-14}

2009/07/14	Janus	43.4±3.3	-3.9±3.5		3.1±1.7		3.3±1.3	671^{+94}_{-111}	69^{+47}_{-24}
2009/07/26	Janus	38.2±1.6	-5.0±1.3		2.5±0.5		3.0±0.5	595^{+86}_{-55}	71^{+25}_{-14}
2010/08/21	Janus	37.7±2.2	-3.5±1.5		3.3±0.5		3.8±0.6	585^{+40}_{-40}	90^{+20}_{-15}
2011/11/10	Janus	37.6±4.0	-6.5±4.2	1.6±0.7	1.2±0.1	3.5±0.7	3.1±0.5	561^{+43}_{-26}	89^{+14}_{-11}
2011/11/12	Janus	37.7±2.7	-5.6±3.3		2.8±0.6	3.5±0.5	4.0±0.7	546^{+53}_{-30}	110^{+25}_{-15}
2011/11/12	Janus	38.8±2.1	-5.8±2.7	2.0±0.4	3.0±0.6	3.6±0.7	3.9±0.8	608^{+43}_{-81}	91^{+31}_{-8}
2012/11/05	Janus	32.2±3.5	-3.2±3.6		1.4±0.6	2.5±0.4	2.7±0.4	591^{+38}_{-72}	69^{+29}_{-9}
2013/02/25	Janus	39.8±1.3	-3.9±1.9		2.9±0.7	3.0±0.7	2.6±0.6	770^{+238}_{-205}	52^{+48}_{-18}
2004/05/30	Kanehekili	32.0±1.6	-18.5±2.2		9.0±1.3		16.3±2.4		
2005/01/15	Kanehekili	32.3±2.4	-17.9±2.2		9.4±1.6		22.1±5.0	382^{+42}_{-26}	1595^{+1075}_{-609}
2005/01/17	Kanehekili	38.3±1.5	-17.3±1.5		5.4±1.0		8.6±1.9	477^{+26}_{-38}	298^{+155}_{-50}
2010/08/21	Kanehekili	32.0±2.2	-18.5±1.5		25.3±3.8		34.2±5.1	520^{+30}_{-30}	990^{+250}_{-170}
2011/11/10	Kanehekili	31.6±3.1	-19.8±3.5	3.4±1.1	5.2±0.9	9.4±1.8	12.5±2.1	468^{+26}_{-23}	475^{+134}_{-81}
2011/11/12	Kanehekili	32.1±3.0	-19.3±3.3		8.3±1.5	11.1±1.9	17.1±2.8	461^{+27}_{-22}	651^{+192}_{-112}
2011/11/12	Kanehekili	33.0±2.7	-19.3±2.8	6.7±1.5	9.4±1.8	12.1±2.1	2.2±0.7	670^{+10}_{-13}	227^{+9}_{-6}
2012/11/05	Kanehekili	28.0±3.5	-15.4±3.4			1.1±0.4	2.9±0.8	286^{+79}_{-38}	994^{+4438}_{-613}
2013/02/25	Kanehekili	34.4±1.7	-16.8±1.6		3.2±1.3	4.4±0.9	3.9±1.1	639^{+108}_{-172}	90^{+156}_{-63}
2012/11/05	Kinich Ahau	310.4±3.9	49.6±3.7			1.1±0.5	1.7±0.3	412^{+136}_{-65}	93^{+185}_{-43}
2007/04/03	Kurdalagon	217.1±1.0	-49.5±1.3		3.5±1.4		6.0±1.3	454^{+62}_{-36}	240^{+140}_{-81}
2007/04/08	Kurdalagon	221.9±2.3	-47.0±2.7		2.4±1.1		6.5±1.2	358^{+31}_{-20}	615^{+360}_{-219}
2011/11/11	Kurdalagon	218.2±2.4	-49.2±2.9		3.2±0.8	3.3±0.6	5.0±1.7	432^{+296}_{-86}	225^{+839}_{-115}
2016/01/22	Kurdalagon	216.5±3.2	-48.8±3.1		2.5±0.5		3.4±0.6	617^{+45}_{-55}	79^{+24}_{-29}
2003/03/09	Loki	311.9±0.4	13.4±1.1		20.1±3.4				
2004/05/28	Loki	309.4±0.6	14.0±1.0		14.5±2.2		41.0±6.0		
2005/05/31	Loki	310.0±1.0	15.0±1.0		10.7±2.6		49.0±9.0	265^{+40}_{-30}	28000^{+77000}_{-15000}
2007/04/03	Loki	305.3±1.6	12.8±1.5		3.9±1.6		16.5±3.2	291^{+19}_{-13}	4945^{+3284}_{-1926}
2007/04/08	Loki	309.1±2.1	13.5±2.3		1.8±0.9		17.4±3.1	259^{+2}_{-8}	12016^{+190}_{-100}
2007/08/14	Loki				2.5±0.4		11.3±1.7	267^{+30}_{-20}	6000^{+9000}_{-3000}
2008/05/11	Loki Patera	309.5±0.4	12.7±0.4	0.37±0.08	16.4±3.3		52.0±10.0	311^{+25}_{-20}	10000^{+7000}_{-4000}
2009/07/24	Loki Patera	307.3±2.8	13.0±2.5	4.32±1.0	82.1±16.1		152.7±25.8	433^{+37}_{-26}	6935^{+2944}_{-1921}
2009/07/26	Loki Patera	311.8±1.3	12.3±1.6		25.3±5.7		45.0±7.5	445^{+38}_{-26}	1896^{+758}_{-511}
2009/08/16	Loki Patera	306.9±0.4	11.3±0.4	4.5±0.7	95.0±14.0		195.0±30.0	392^{+30}_{-20}	12600^{+5600}_{-3700}
2009/09/10	Loki Patera	310.6±0.4	11.3±0.4	4.4±0.7	110±17		177±26	456^{+35}_{-30}	6900^{+2500}_{-1600}
2010/07/27	Loki Patera	306.5±2.5	16.0±1.7		31.8±4.8		44.8±6.7	478^{+95}_{-60}	1600^{+1200}_{-500}
2010/08/21	Loki Patera				38±6		64±10	443^{+85}_{-55}	2700^{+2600}_{-1000}
2010/09/09	Loki Patera	308.4±1.4	15.2±1.4		45±7		130±25	325^{+50}_{-35}	20000^{+30000}_{-9000}
2010/09/18	Loki Patera	308.1±1.4	16.0±1.4		62±9		230±35	290^{+30}_{-25}	70000^{+9000}_{-3000}
2010/09/20	Loki Patera	306.6±2.0	16.3±2.0		97±15		143±22	486^{+100}_{-65}	4800^{+3900}_{-1500}
2011/07/28	Loki Patera	308.6±0.6	12.8±0.7		13.8±2.1		41.6±6.3	337^{+40}_{-30}	5200^{+5400}_{-2100}
2011/11/10	Loki Patera	310.3±2.5	13.6±2.6	10.6±2.2	19.9±4.5	25.3±4.3	34.3±5.7	476^{+22}_{-19}	1239^{+291}_{-176}
2011/11/12	Loki Patera	314.7±2.9	14.9±3.5		10.8±2.4	19.3±3.2	18.2±4.3	626^{+122}_{-68}	432^{+101}_{-52}
2012/11/05	Loki Patera	308.1±1.5	12.9±2.0		8.2±1.7	11.9±2.2	31.6±5.3	309^{+31}_{-21}	6455^{+5881}_{-2711}
2013/01/20	Loki Patera	310.9±0.4	12.2±1.0		3.6±0.5		17.4±2.6	287^{+25}_{-20}	5700^{+5100}_{-2300}
2013/02/26	Loki Patera	308.5±2.5	14.5±2.6		11.5±4.3	15.9±3.5	24.9±4.3	401^{+45}_{-148}	1468^{+473}_{-254}
2013/02/28	Loki Patera	311.6±2.1	14.8±1.9		11.9±2.5	14.7±3.2	24.7±4.5	428^{+70}_{-120}	1167^{+869}_{-243}
2016/01/22	Loki Patera	306.7±2.9	14.4±3.0	6.61±2.0	91.5±18.7		152.0±39.5	467^{+67}_{-47}	5598^{+4125}_{-1879}
2004/05/27	Mailk	131.7±1.6	-31.8±1.4		1.2±0.3		1.7±0.3		
2003/01/26	Malik	124.4±1.6	-31.9±1.3		3.2±0.8		6.0±1.3	435^{+51}_{-31}	274^{+150}_{-91}
2005/01/17	Malik	126.9±2.1	-32.5±1.8		1.4±0.3		2.6±0.4	434^{+44}_{-28}	118^{+56}_{-36}
2007/09/09	Malik	130.1±0.8	-34.6±1.4		1.2±0.3		2.3±0.5	431^{+54}_{-29}	108^{+55}_{-37}
2008/10/06	Malik	131.7±1.6	-32.6±2.0		1.4±0.7		1.8±0.3	563^{+61}_{-41}	46^{+14}_{-8}
2010/07/28	Malik	128.1±2.5	-32.7±1.7		1.8±0.3		2.7±0.4		
2012/11/04	Malik	128.4±2.6	-33.0±2.6		0.8±0.7	1.1±0.3	1.6±0.6	451^{+652}_{-100}	65^{+282}_{-25}
2004/05/29	Marduk Fluctus	211.0±1.9	-22.2±2.6		2.2±0.6		3.1±0.5		
2007/04/03	Marduk Fluctus	208.9±2.3	-23.3±2.2		2.5±0.8		4.5±0.9	450^{+53}_{--30}	183^{+84}_{-57}
2007/09/09	Marduk Fluctus	199.7±2.2	-23.6±2.0				2.9±0.8		
2008/10/06	Marduk Fluctus	209.9±2.5	-23.6±2.5		3.0±1.3		4.6±0.8	490^{+61}_{-34}	152^{+62}_{-42}
2009/07/16	Marduk Fluctus	204.9±1.2	-23.5±1.8		2.8±1.0		3.7±0.9	547^{+119}_{-60}	98^{+56}_{-30}
2009/07/25	Marduk Fluctus	210.6±1.4	-25.6±1.6		4.0±1.3		4.0±0.6	691^{+111}_{-64}	84^{+18}_{-10}
2010/08/22	Marduk Fluctus	210.3±2.5	-24.0±1.7		3.1±0.5		3.4±0.5	635^{+170}_{-1}	70^{+3}_{-7}
2011/11/11	Marduk Fluctus	210.6±2.2	-26.7±2.6	3.4±1.2	4.9±1.1	6.8±1.1	6.2±1.0	569^{+38}_{-24}	171^{+19}_{-28}
2013/02/26	Marduk Fluctus	212.3±1.4	-23.4±1.7		2.0±0.9	2.2±0.6	2.0±0.4	746^{+754}_{-166}	42^{+37}_{-16}
2013/03/01	Marduk Fluctus	198.4±3.6	-22.9±3.4		5.3±1.6	4.3±0.5	5.5±1.5	580^{+1137}_{-154}	123^{+342}_{-70}
2016/01/22	Marduk Fluctus	212.3±3.9	-23.9±4.1		7.6±1.9		10.7±3.0	537^{+137}_{-82}	273^{+275}_{-89}
2003/01/26	Masubi	56.0±1.9	-42.7±1.9		7.5±1.2		9.6±1.7	558^{+70}_{-43}	244^{+81}_{-54}
2004/05/30	Masubi	58.8±2.3	-43.5±2.0		3.9±0.6		6.8±1.0		
2005/01/15	Masubi	53.4±1.5	-43.2±2.0		4.2±1.3		8.8±1.5	405^{+35}_{-24}	504^{+241}_{-156}
2005/01/17	Masubi	61.9±1.2	-41.7±1.4		3.9±1.2		6.9±1.1	446^{+37}_{-26}	286^{+107}_{-74}
2008/10/09	Masubi	60.6±0.6	-46.6±1.2		2.3±0.6		3.8±0.7	469^{+60}_{-33}	141^{+66}_{-43}
2009/07/26	Masubi	55.6±1.1	-47.6±1.4				2.2±0.6		
2010/08/21	Masubi	54.1±4.5	-44.2±2.5		1.8±0.4		3.0±0.5	465^{+35}_{-70}	110^{+130}_{-40}
2011/11/12	Masubi	55.3±3.9	-45.1±4.2		1.9±0.4	2.4±0.6	4.0±0.9	464^{+65}_{-35}	152^{+82}_{-33}
2011/11/12	Masubi	54.2±4.2	-44.8±4.1			2.9±0.5	5.1±1.4	353^{+125}_{-65}	513^{+71}_{-205}
2013/02/25	Masubi	56.2±2.5	-44.4±2.3		3.1±1.1	4.2±1.1	3.6±0.7	625^{+209}_{-170}	84^{+403}_{-24}
2009/07/25	Mulungu	218.8±0.7	20.0±1.4				1.3±0.2		

2010/08/22	Mulungu	217.5±2.5	17.0±1.7			6.0±0.9		12.3±1.8	410^{+55}_{-40}	670^{+550}_{-230}
2011/11/11	Mulungu	218.4±2.1	15.0±2.5		1.4±0.3	2.2±0.4	3.4±0.6	3.1±0.4	537^{+16}_{-16}	95^{+11}_{-7}
2013/02/26	Mulungu	217.5±1.4	17.4±1.7				4.0±0.6	2.8±0.8	642^{+853}_{-74}	67^{+24}_{-19}
2012/11/05	N. Lerna Region	297.2±3.5	-49.6±3.2			2.6±0.8	5.0±1.0	5.5±1.0	575^{+108}_{-64}	142^{+62}_{-31}
2007/09/09	NIMSI32D	177.3±1.4	-42.0±1.7					5.7±1.5		
2008/10/06	NIMSI32D	174.1±1.9	-40.2±2.4			1.5±0.4		1.4±0.4	749^{+255}_{-110}	29^{+10}_{-1}
2009/07/16	NIMSI32D	172.5±1.3	-42.7±1.4			1.0±0.5		1.2±0.2	627^{+166}_{-67}	26^{+9}_{-5}
2012/11/04	NIMSI32J	83.5±2.4	-18.8±2.1			2.1±0.9	2.7±0.6	4.6±1.1	458^{+136}_{-59}	179^{+186}_{-72}
2010/07/28	P98	148.9±2.5	-15.0±1.7					0.8±0.1		
2003/01/26	P207	97.0±1.5	-36.2±2					1.6±0.2		
2007/04/03	Pele	253.3±1.0	-17.9±1.1			5.3±1.1		6.1±1.0	613^{+83}_{-55}	139^{+42}_{-25}
2007/04/08	Pele	257.1±2.4	-18.0±2.1			6.0±1.8		9.5±2.0	479^{+67}_{-40}	327^{+7}_{-}
2007/08/14	Pele					4.8±0.7		4.8±0.7		
2009/07/25	Pele	252.4±1.2	-18.2±1.8			3.6±1.0		5.1±0.8	518^{+60}_{-36}	149^{+52}_{-35}
2010/07/27	Pele					2.1±0.3		2.1±0.3		
2010/08/22	Pele	252.0±3.3	-17.2±1.7			8.0±1.2		8.3±1.3		
2010/09/09	Pele					6.0±0.9		9.3±1.5		
2010/09/18	Pele					1.0±0.2				
2011/07/28	Pele					1.6±0.3		3.5±0.6		
2011/11/11	Pele	252.3±3.1	-18.1±3.2				5.9±1.0			
2013/01/20	Pele			2±1		4.5±0.7		5.7±0.9		
2013/02/26	Pele	254.8±1.9	-17.8±1.8			4.9±1.0	6.2±1.4	4.9±1.2	722^{+211}_{-254}	105^{+299}_{-18}
2013/02/28	Pele	258.8±1.7	-17.3±2.1			2.8±0.6	4.6±1.0	3.1±0.6	613^{+309}_{-74}	86^{+16}_{-21}
2016/01/22	Pele	255.4±2.3	-18.2±2.6			1.1±0.3		2.3±0.6	496^{+210}_{-74}	75^{+81}_{-14}
2008/10/09	PFd224	99.8±1.7	-38.3±1.4					4.9±1.0		
2009/07/14	PFd224	100.3±2.7	-37.1±3.1			1.2±0.4		1.8±0.4	506^{+97}_{-50}	57^{+34}_{-19}
2009/07/16	PFd224	99.3±2.2	-37.9±2.0					1.6±0.5		
2008/10/06	PFd267	109.3±1.7	-35.6±2.3					4.3±0.8		
2013/03/01	PFd267	110.8±3.2	-48.1±3.6					2.7±0.7	863^{+516}_{-171}	53^{+15}_{-26}
2005/01/17	PFu374	63.5±1.8	-24.3±2			3.1±0.8		2.4±0.5	927^{+71}_{-132}	50^{+17}_{-35}
2005/01/15	PFd535	59.6±0.9	-7.4±1.5					1.7±0.3		
2009/07/14	PFd535	67.7±2.4	-9.0±2.1					1.0±0.2		
2009/07/26	PFd535	60.3±1.8	-9.6±1.8					0.7±0.1		
2009/07/14	PFd681	95.4±2.3	6.6±2.4			2.1±0.5		2.7±0.6	557^{+94}_{-48}	70^{+29}_{-17}
2009/07/16	PFd681	98.0±1.8	4.3±2.5			2.1±0.5		3.1±0.6	503^{+77}_{-43}	95^{+48}_{-28}
2005/01/15	PFd717	54.2±1.9	10.0±2.1			1.5±0.8		1.1±0.3	1003^{+155}_{-219}	24^{+107}_{-106}
2011/11/12	PFd717	58.9±4.6	9.3±4.3			1.3±0.4	0.8±0.2	1.1±0.3	860^{+96}_{-157}	22^{+7}_{-6}
2009/07/16	Pfu1410	185.9±1.1	-5.9±1.4			1.1±0.2		3.9±0.7	315^{+25}_{-15}	717^{+442}_{-282}
2009/07/25	Pfu1410	187.2±1.8	-5.4±1.6			1.3±0.2		4.0±0.6	341^{+23}_{-16}	485^{+249}_{-155}
2010/07/28	Pfu 1410	186.1±2.5	-5.0±1.5			0.5±0.1		1.4±0.2		
2011/11/11	Pfu1410	179.8±3.4	-7.3±4.1				0.8±0.2	1.5±0.2	345^{+28}_{-19}	168^{+99}_{-41}
2005/01/15	PFd1746	5.0±1.8	-10.8±1.6			7.5±1.9		22.2±4.2	339^{+26}_{-17}	2759^{+1625}_{-981}
2007/04/03	Pillan							1.0±0.2		
2004/05/29	Pillan	241.4±2.3	-11.4±2.0			3.6±1.1		11.6±2.4		
2007/04/08	Pillan	244.4±1.5	-8.5±1.5	25.6±7.3		34.5±6.4		45.6±7.8	759^{+127}_{-196}	794^{+736}_{-104}
2007/08/14	Pillan					30.3±4.5		23.2±3.5	840^{+40}_{-40}	490^{+30}_{-30}
2009/07/25	Pillan							1.1±0.2		
2010/06/28	Pillan					23.0±4.0		25.0±4.0	640^{+200}_{-100}	540^{+300}_{-70}
2010/07/27	Pillan							2.0±1.0		
2010/08/22	Pillan	242.0±3.3	-12.0±1.7			2.4±0.4		5.8±0.9	375^{+40}_{-40}	450^{+500}_{-200}
2010/09/09	Pillan					2.0±0.3		9.5±1.5	275^{+25}_{-25}	5000^{+7000}_{-2000}
2011/07/28	Pillan							2.4±0.4		
2011/11/11	Pillan	242.3±3.2	-13.7±3.9			0.7±0.2	3.2±0.7	2.3±0.4	717^{+48}_{-18}	53^{+2}_{-6}
2013/01/20	Pillan							2.0±0.3		
2013/02/26	Pillan	245.0±2.2	-11.8±2			3.9±1.1	4.0±0.8	5.3±1.1	514^{+146}_{-109}	154^{+304}_{-55}
2015/02/18	Pillan					80±16				
2015/03/15	Pillan					20±10				
2003/03/08	Prometheus	156.3±0.9	-0.6±1.6			3.3±0.6		5.5±1.1	459^{+58}_{-35}	215^{+112}_{-68}
2004/05/27	Prometheus	156.9±0.6	-0.8±1.3			3.1±0.5		3.9±0.6		
2004/05/29	Prometheus	158.4±2.5	-0.8±2.2			2.1±0.5		2.4±0.5		
2005/01/17	Prometheus	151.3±1.4	-0.3±1.7			1.9±0.9		3.7±1.1	422^{+87}_{-41}	183^{+178}_{-82}
2007/09/09	Prometheus	156.5±1.4	-1.5±1.4			1.9±0.5		4.9±1.4	367^{+53}_{-28}	415^{+369}_{-188}
2008/10/06	Prometheus	155.9±2.1	-1.2±2.0			2.6±0.5		3.9±0.7	501^{+51}_{-77}	123^{+123}_{-30}
2009/07/14	Prometheus	151.0±2.0	-2.1±2.3			2.0±0.7		3.1±0.8	476^{+78}_{-42}	112^{+68}_{-38}
2009/07/16	Prometheus	153.1±0.9	-1.9±1.5			2.0±0.4		3.1±0.5	490^{+82}_{-47}	103^{+62}_{-33}
2009/07/25	Prometheus	153.8±1.0	-1.8±1.6			3.0±0.7		4.2±0.7	516^{+59}_{-41}	125^{+50}_{-31}
2010/07/28	Prometheus	152.5±2.5	-1.5±1.7			1.6±0.2		2.4±0.4	500^{+85}_{-60}	80^{+45}_{-25}
2011/11/11	Prometheus	154.3±2.3	-3.4±2.4		0.6±0.3	2.4±0.5	4.1±0.8	3.9±0.6	529^{+19}_{-18}	118^{+16}_{-10}
2012/11/04	Prometheus	153.2±2.2	-2.2±2.4			2.1±0.8	2.7±0.6	3.7±0.6	478^{+84}_{-24}	129^{+1}_{-46}
2013/03/01	Prometheus	155.9±1.7	-1.6±1.5			3.4±1.6	2.7±0.5	3.2±0.6	575^{+514}_{-84}	76^{+51}_{-1}
2007/04/03	S. of Babbar	282.1±3.7	-52.9±3.4			4.0±1.5		5.9±1.2	505^{+68}_{-39}	180^{+77}_{-50}
2007/04/08	S. of Babbar	286.5±2.2	-53.0±2.3			2.8±1.0		4.8±1.8	459^{+153}_{-56}	184^{+217}_{-86}
2016/01/22	S. of Babbar	288.3±3.4	-49.0±3.9			1.8±0.3		3.1±0.5	509^{+113}_{-62}	96^{+67}_{-28}

2011/11/11	Shamash	153.1±3.3	-34.0±3.7			1.5±0.4	3.5±0.8	3.4±0.6	549^{+58}_{-35}	93^{+30}_{-14}
2012/11/04	Shango	100.6±1.7	31.9±2.2		3.5±1.1	4.4±1.2	6.3±1.5	8.6±1.5	471^{+67}_{-43}	312^{+181}_{-94}
2013/02/25	Shango	100.6±2.0	32.3±2.1			3.7±0.9	4.7±0.9	5.4±0.9	505^{+76}_{-109}	167^{+361}_{-53}
2013/03/01	Shango	105.0±1.6	33.3±2.0			6.1±2.6	5.9±1.0	6.2±2.1	689^{+1025}_{-258}	127^{+820}_{-63}
2005/01/17	Sigurd	97.3±2.4	-2.4±2.1					1.5±0.3		
2004/05/27	Sigurd	101.1±1.4	-4.8±1.3			0.6±0.1		1.9±0.4		
2004/05/27	Sobo	151.5±3.3	17.8±3.3			0.5±0.1		0.7±0.4		
2008/10/06	Sobo	152.7±1.4	16.4±2.0			1.5±0.9		1.2±0.4	925^{+120}_{-192}	25^{+7}_{-22}
2012/11/04	Sobo	149.9±2.5	12.9±2.8			1.3±0.5	1.2±0.3	1.2±0.3	740^{+528}_{-205}	25^{+31}_{-5}
2008/10/09	Sui Jen	-2.5±1.6	-19.2±1.7			6.1±1.1		12.6±3.0	410^{+50}_{-31}	689^{+461}_{-255}
2003/03/09	Surt	337.5±1.3	46.2±1.9			1.4±0.8				
2012/11/05	Surt	335.4±2.9	44.5±3.1		1.5±0.3	1.3±0.4	1.9±0.3	2.1±0.3	573^{+98}_{-65}	51^{+23}_{-11}
2009/07/16	Surya	144.5±2.2	21.2±1.9			1.1±0.3		1.4±0.3	572^{+129}_{-65}	35^{+20}_{-9}
2003/01/26	Tawhaki	75.0±1.3	3.7±1.8			1.7±0.3		2.3±0.4	519^{+74}_{-43}	69^{+30}_{-19}
2004/05/27	Tawhaki	82.5±2.2	3.2±2.2			1.8±0.5		1.1±0.3		
2005/01/15	Tawhaki	74.0±1.3	3.8±1.5			1.3±0.2		2.1±0.4	473^{+53}_{-33}	74^{+32}_{-21}
2005/01/17	Tawhaki	75.1±1.6	4.1±1.6			2.0±0.6		4.9±0.9	372^{+34}_{-22}	389^{+230}_{-137}
2008/10/09	Tawhaki	77.0±1.1	3.3±1.4			1.4±0.8		1.0±0.3	1010^{+149}_{-224}	23^{+4}_{-2}
2009/07/14	Tawhaki	77.4±2.6	3.3±2.3			1.2±0.3		1.4±0.3	645^{+128}_{-67}	30^{+9}_{-5}
2009/07/26	Tawhaki	73.4±1.5	2.6±1.7			1.3±0.2		1.3±0.1	681^{+48}_{-74}	28^{+7}_{-2}
2010/08/21	Tawhaki	73.3±4.5	4.6±2.5			0.8±0.1		0.9±0.1		
2011/11/12	Tawhaki	74.1±3.1	2.3±3.3		0.9±0.1	1.2±0.3	1.3±0.3	1.1±0.2	656^{+55}_{-28}	29^{+2}_{-4}
2012/11/04	Tawhaki	78.1±2.7	2.7±3.0			1.4±0.3	1.7±0.4	1.9±0.3	585^{+176}_{-83}	47^{+27}_{-10}
2013/02/25	Tawhaki	77.3±1.9	3.2±1.7			7.9±2.4	9.8±1.7	12.4±2.1	487^{+120}_{-62}	412^{+338}_{-140}
2013/03/01	Tawhaki	81.6±1.6	3.8±1.9			5.2±1.7	3.7±0.8	6.8±2.4	546^{+267}_{-166}	175^{+129}_{-72}
2003/03/08	Thor	135.0±2.1	38.3±2.1			1.5±0.4		2.0±0.4	554^{+81}_{-48}	51^{+19}_{-12}
2008/10/06	Thor	137.5±1.4	38.6±2.0			1.3±0.3		0.9±0.3	1133^{+159}_{-273}	22^{+32}_{-15}
2009/07/14	Thor	129.5±2.1	36.9±2.5			0.7±0.1		0.7±0.1	691^{+73}_{-49}	16^{+2}_{-1}
2009/07/16	Thor	132.7±1.8	39±2.0			0.7±0.1		1.3±0.2	467^{+71}_{-36}	47^{+25}_{-15}
2012/11/05	Tol Ava	326.5±2.7	1.1±2.9			0.7±0.2	1.3±0.4	1.2±0.3	527^{+241}_{-87}	36^{+43}_{-12}
2004/05/28	Tung Yo	-1.9±1.6	-17.3±1.5			72.0±12.0		94.0±15.0		
2003/03/08	Tupan	141.8±0.9	-18.8±1.4	10.2±5.6		19.2±3.0		27.8±4.8	579^{+86}_{-12}	647^{+19}_{-31}
2004/05/27	Tupan	142.9±2.2	-16.4±2.5			2.5±0.8		2.9±0.8		
2005/01/17	Tupan	139.7±1.1	-17.5±1.6			2.6±1.0		2.8±0.5	645^{+128}_{-67}	60^{+19}_{-11}
2007/09/09	Tupan	142.9±2.0	-18.1±1.9			3.0±1.2		3.9±1.1	556^{+149}_{-58}	100^{+53}_{-31}
2008/10/06	Tupan	142.9±1.9	-18.2±2.0			1.9±0.7		1.5±0.7	874^{+185}_{-205}	31^{+50}_{-16}
2009/07/14	Tupan	137.3±1.8	-17.7±2.5			1.4±0.5		1.1±1.0	815^{+183}_{-235}	24^{+35}_{-7}
2009/07/16	Tupan	139.3±1.8	-18.5±1.8			1.2±0.2		1.9±0.5	481^{+113}_{-104}	65^{+182}_{-26}
2010/07/28	Tupan	139.7±2.5	-17.5±1.7			0.8±0.1		1.0±0.2		
2011/11/11	Tupan	143.1±3.9	-20.3±4.0			1.3±0.3	3.0±1.0	1.2±0.2	900^{+149}_{-79}	47^{+33}_{-28}
2012/11/04	Tupan	140.8±2.6	-18.6±2.8			1.0±0.3	1.2±0.3	2.2±0.4	339^{+45}_{-27}	274^{+277}_{-122}
2013/03/01	Tupan	143.7±1.2	-18.0±1.7			2.0±0.8	1.5±0.4	1.5±0.5	990^{+418}_{-161}	29^{+160}_{-17}
2007/09/09	Tvashtar	130.4±2.1	60.7±2.2	35.7±18.8		40.8±9.0		38.0±6.8	912^{+197}_{-243}	715^{+324}_{-61}
2003/03/09	Ukko	11.5±1.1	35.0±1.4			1.3±0.4				
2007/04/03	Ulgen	286.1±2.0	-36.3±1.8			3.2±0.8		1.6±0.3		
2007/04/08	Ulgen	288.7±2.2	-37.4±2.0			3.0±1.2		6.9±1.2	384^{+33}_{-22}	482^{+248}_{-159}
2012/11/05	Ulgen	292.2±3.3	-35.0±3.6		1.8±0.7	2.2±0.6	4.2±0.7	2.6±0.6	618^{+88}_{-61}	80^{+24}_{-12}
2016/01/22	Ulgen	286.1±3.0	-38.5±2.9			1.8±0.3		3.1±0.7	454^{+150}_{-67}	121^{+175}_{-52}
2008/10/09	Unidentified23W	25.6±0.8	4.3±1.3			1.6±0.8		3.1±0.7	437^{+82}_{-32}	137^{+78}_{-56}
2009/07/26	Unidentified23W	21.8±1.8	4.6±1.6			1.1±0.4		1.6±0.3	528^{+79}_{-33}	45^{+13}_{-12}
2003/01/26	Unidentified35W	37.8±1.9	15.4±2.0					2.3±0.6		
2003/03/09	Unidentified6119	312.6±1.3	-28.8±1.4			0.7±0.1				
2012/11/05	Unidentified6119	311.7±2.9	-29.5±3.2		1.6±0.4	1.2±0.3	1.5±0.4	1.5±0.3	749^{+218}_{-123}	30^{+10}_{-1}
2005/01/15	Uta	20.6±1.8	-33.8±1.8			1.6±0.5		4.6±1.5	344^{+61}_{-29}	525^{+671}_{-273}
2008/10/09	Uta	24.2±2.4	-34.8±2.3			2.4±0.8		5.2±1.3	403^{+56}_{-29}	301^{+204}_{-119}
2009/07/26	Uta	21.4±2.0	-35.6±1.7			2.6±0.6		4.4±0.7	464^{+46}_{-30}	168^{+69}_{-45}
2010/08/21	Uta	22.5±2.5	-34.4±1.7			2.3±0.4		5.3±0.8	385^{+55}_{-40}	370^{+370}_{-140}
2011/11/10	Uta	21.9±2.8	-35.8±3.3		1.7±0.7	2.2±0.6	3.4±0.8	4.0±0.7	523^{+18}_{-28}	120^{+30}_{-13}
2011/11/12	Uta	23.1±4.0	-35.6±4.0			3.0±0.7	3.3±0.7	5.3±0.7	463^{+87}_{-46}	199^{+87}_{-46}
2011/11/12	Uta	21.9±2.6	-36.1±3.1			3.0±0.7	3.5±0.6	5.0±0.7	471^{+39}_{-26}	180^{+60}_{-35}
2012/11/05	Uta	17.6±2.9	-32.8±3.4		1.9±0.8	1.9±0.7	3.2±0.9	5.1±0.9	460^{+75}_{-140}	197^{+2617}_{-65}
2013/02/25	Uta	23.7±2.4	-34.7±2.6			3.6±1.1	3.3±0.7	4.4±1.6	583^{+287}_{-158}	106^{+323}_{-32}
2010/07/28	Volund	171.2±2.5	26.0±1.7			2.6±0.4		2.2±0.3	825^{+300}_{-150}	50^{+4}_{-4}
2011/11/11	Volund	174.3±3.6	23.3±3.5			1.5±0.3	1.4±0.3	0.9±0.1	1145^{+347}_{-141}	30^{+13}_{-1}
2013/03/01	Volund	175.8±2.7	26.1±2.5				5.8±0.8	1.6±0.6	1465^{+306}_{-278}	191^{+58}_{-35}
2003/01/26	Zal	75.4±1.5	39.3±1.8			2.2±0.4		3.4±0.6	492^{+50}_{-33}	113^{+41}_{-28}

2005/01/15	Zal	73.9±1.8	38.0±2.3	1.3±0.4		3.8±0.9	341^{+40}_{-23}	451^{+394}_{-198}
2005/01/17	Zal	77.5±1.9	39.0±2.1	1.4±0.5		3.4±0.8	374^{+49}_{-28}	265^{+218}_{-112}
2008/10/09	Zal	79.0±0.9	38.3±1.4	2.7±0.9		4.2±1.2	487^{+100}_{-47}	141^{+95}_{-51}
2009/07/14	Zal	77.6±2.1	36.7±2.7	1.1±0.3		2.1±0.4	437^{+42}_{-27}	97^{+43}_{-28}
2009/07/26	Zal	75.2±1.8	38.6±1.6	1.9±0.7		2.8±0.5	516^{+82}_{-41}	81^{+34}_{-23}
2010/08/21	Zal	73.3±4.5	40.0±2.5	6.2±0.9		6.2±0.9	690^{+200}_{-105}	130^{+40}_{-10}
2011/11/12	Zal	72.9±3.2	36.6±3.1	1.5±0.3	2.9±0.7	2.9±0.6	560^{+64}_{-40}	78^{+22}_{-12}
2011/11/12	Zal	74.5±4.4	37.4±4.8		3.1±0.7	3.6±0.8	564^{+108}_{-113}	90^{+83}_{-21}
2012/11/04	Zal	79.0±3.4	37.0±3.4	2.5±0.6	3.2±0.9	3.4±1.0	558^{+48}_{-60}	88^{+23}_{-24}
2012/02/25	Zal	76.9±2.5	37.6±2.2	3.0±0.6	3.6±0.5	3.1±0.7	684^{+213}_{-138}	68^{+41}_{-21}
2003/03/08	Zamama	173.5±1.1	17.3±1.6	1.2±0.3		1.8±0.3	490^{+65}_{-39}	62^{+29}_{-18}
2004/05/29	Zamama	174.4±2.8	15.8±2.5	1.3±0.5		1.9±0.4		
2007/09/09	Zamama	174.3±3.2	16.9±2.9	1.3±0.7		2.5±1.3	434^{+250}_{-60}	113^{+206}_{-63}
2008/10/06	Zamama	174.1±2.1	14.8±2.2	1.3±0.5		0.5±0.2		